

Impact of lateral groundwater flow on hydrothermal conditions of the active layer in a high arctic hillslope setting

Alexandra Hamm^{1,2} and Andrew Frampton^{1,2}

¹Department of Physical Geography, Stockholm University, Stockholm, Sweden

²Bolin Centre for Climate Research, Stockholm University, Stockholm, Sweden

Correspondence: Alexandra Hamm (alexandra.hamm@natgeo.su.se)

Abstract. Modeling the physical state of permafrost landscapes is a crucial addition to field observations in order to understand its feedback mechanisms the feedback mechanisms between permafrost and the atmosphere within a warming climate. A common hypothesis in permafrost modeling is that vertical heat conduction is most relevant to derive subsurface temperatures. While this approach is mostly applicable to flat landscapes with little topography, landscapes with more topography are subject 5 to lateral flow process as well. With our study, we want to contribute to the growing body of evidence that lateral surface- and subsurface processes can have a significant impact on permafrost temperatures and active layer properties. We use a numerical model to simulated simulate two idealized hillslopes (a steep and a medium case) with inclinations that can be found in Adventdalen, Svalbard, and compare them to a flat control case. We find that ground temperatures within the active layer uphill are generally warmer than downhill in both slopes (with a difference of up to 1.20.8°C in the steep, and 0.70.6°C in the 10 medium slope). Further, the slopes are found to be warmer in the uphill section and colder in the very bottom base of the slopes compared to the flat control case. As a result, maximum thaw depth increases by about 5 cm from the flat (750.98 emm) to the steep slope (80medium (1.03 em), while the medium case does not exhibit a deepening in thaw depth (75m) and the steep slope (1.03 emm). Uphill warming on the slopes is explained by overall lower heat capacity, additional energy gain through infiltration, and lower evaporation rates due to a overall drier environment drier conditions caused by subsurface runoff. The 15 major governing process causing the cooling on the downslope side is heat loss to the atmosphere through evaporation in summer and enhanced heat loss in winter due to wetter conditions and resulting higher increased thermal conductivity. On a catchment scale, these results suggest that temperature distributions in hilly sloped terrain can vary considerably compared to flat terrain, which might change impact the response of subsurface hydrothermal conditions to ongoing climate change.

1 Introduction

20 Permafrost is defined as ground that remains below 0 °C for at least two consecutive years. It covers approximately 24% of the exposed land area in the northern hemisphere (Zhang et al., 1999) and stores about 1030 Pg of organic carbon in the upper 3 meters of soil (Hugelius et al., 2014). With increasing air temperatures in the Arctic, this carbon stock gets thawed out of the permafrost, exposing it to microbial decomposition and displacement. How much carbon gets released from the permafrost is strongly influenced by the depth of the active layer, the part of the soil that seasonally thaws out (e.g., Bisk-

25 aborn et al., 2019). The correlation between increasing air temperature and depth of the active layer is well established (e.g., Zhang et al., 1997; Isaksen et al., 2007; Frauenfeld et al., 2004). Especially high summer temperatures in dry environments have a direct impact on the development of the active layer in the same year (Isaksen et al., 2007). However, the effect of precipitation and hydrology in the active layer are less well understood as their effects are more dynamic and non-linear (e.g., Wen et al., 2014). Due to the ~~water impermeability~~ ~~low permeability~~ of frozen ground, relevant hydrological processes are limited to the active layer. With increasing active layer thicknesses, more water can infiltrate into the ground and move laterally. The degradation of permafrost has found to decrease the seasonal variability of groundwater discharge into surface waters, changing the hydraulic connectivity in the subsurface and potentially also the solute transport capabilities (Frampton et al., 2011, 2013; Evans and Ge, 2017; McKenzie et al., 2021) (Frampton et al., 2011, 2013; Frampton and Destouni, 2015; Evans et al., 2016). Further, higher moisture abundance in the active layer ~~can not only regulate~~ ~~regulates~~ the decomposition of organic carbon (e.g., McGuire et al., 2009; Koven et al., 2011) ~~but and~~ can also affect infrastructure built on the fragile frozen ground (e.g., de Grandpré et al., 2012) ~~or and~~ change the thermal properties of the permafrost (e.g., Schuh et al., 2017). Therefore, it is important to investigate the effect of ~~hydrology~~ ~~hydrological and hydrogeological processes~~ in permafrost landscapes.

40 In general, it is known that the amount of liquid water in the soil has a direct effect on its thermal properties (e.g., Iijima et al., 2010; Zhu et al., 2017). ~~Higher saturated~~ ~~Wet~~ soils are expected to conduct more heat towards the subsurface than ~~drier~~ ~~dry~~ soils in summer and, depending on the insulating effect of the snow cover, loose ~~more~~ energy to the atmosphere in winter (Kane et al., 2001). These conclusion are often based on 1D ~~column~~ representations of permafrost soils due to the assumption that vertical heat conduction is the major control of energy fluxes. For flat landscapes with little topography and low hydraulic gradients, these assumptions might be sufficient (Westermann et al., 2016; Langford et al., 2020). However, for permafrost underlying slopes ~~and landscapes with more topography~~, vertical conduction alone ~~is not~~ ~~might not be~~ able to 45 explain permafrost degradation and seasonal active layer thaw. Due to the slopes and ~~associated~~ hydraulic gradients, lateral advection of water and energy might ~~change the ground temperature between the~~ ~~impact the ground thermal regime between~~ up- and downhill ~~location~~ ~~locations~~. Especially in warmer, discontinuous permafrost landscapes, heat carried laterally by water has proven to be essential for subsurface temperatures and permafrost thaw (Sjöberg et al., 2016; Kurylyk et al., 2016; de Grandpré et al., 2012). This effect is even more enhanced and prolonged if water is gathering in water tracks on hillslopes (Evans et al., 50 2020). In a controlled laboratory experiment it was also found that subsurface flow can greatly enhance active layer thaw, but highly depends on the water temperature (Veuille et al., 2015). Further, ~~Groundwater~~ ~~groundwater~~ flow along a hillslope in combination with preferential snow accumulation has shown how water and heat transport affect the emergence of a talik and how the talik can change the hydrological pathways within a permafrost hillslope (Jafarov et al., 2018).

55 In high Arctic continuous permafrost landscapes, the effect of subsurface flow is expected to be less ~~strong~~ ~~significant~~ due to thin organic layers and generally low hydraulic conductivities (Loranty et al., 2018). In Yukon, Canada, it has been observed that vertical heat advection through snow-melt and summer rain infiltration on a road embankment change subsurface temperatures faster than through heat conduction from the surface (Chen et al., 2020).

~~In this study, we investigate the role of hydrology on two high Arctic hillslopes and its effects on the active layer and ground temperatures, using a physically-based numerical model.~~ Understanding and quantifying local-scale hydraulic permafrost pro-

60 cesses helps to better constrain and inform global climate models and the feedback mechanisms between permafrost landscapes and the atmosphere, as permafrost is a key component of the climate system (Riseborough et al., 2008; Schuur et al., 2015). While field measurements are a vital source to achieve this, numerical modeling allows for applications ~~in more remote and less accessible areas with varying scenarios regarding environmental factors, such as climate setting or slope inclination. Further, modeling can help untangling potential non-linear effects in the domain and dissect energy fluxes, which can be complex to~~
65 measure in the field.

In this study, we investigate the role of hydrology on two idealized, 50 m long, high Arctic hillslopes and its effects on the active layer and ground temperatures, using a two-dimensional physically-based numerical model. We conducted a series of numerical model investigations representing typical hillslope environments and hydro-meteorological conditions of Adventdalen, Svalbard. Svalbard is located at 78°N and 15°E and therefore represents high-Arctic climate. Active layer thickness 70 in Adventdalen has shown to increase with a rate of 0.7 cm yr^{-1} over the last decades (Strand et al., 2020). The location of Adventdalen in close vicinity to Svalbard's main settlement Longyearbyen further paves the way to validate model results with field measurements due to relatively easy access. The hillslopes are represented as idealized slopes with a steep (22°) and medium (11°) inclination and are compared to a reference case without inclination (flat case). We focus on absolute temperature differences between the uphill and downhill side in the slopes at several different depths within the active layer as well as 75 the transect-wide active layer thickness in all cases.

The model is controlled and driven by ~~site-specific~~ hydro-meteorological data and subsurface properties. ~~The data represents current climatic conditions in Svalbard are consistent with site conditions~~. Our objectives are to understand and quantify the effects hillslope inclination have on active layer thermal and hydraulic dynamics of a permafrost catchment.

Specifically, the following questions are investigated: (i) To ~~which~~ what extent does hillslope inclination affect the ground 80 temperatures in a permafrost catchment? (ii) ~~To which~~ To what extent is maximum active layer thickness and the volume of unfrozen soil affected by those differences? (iii) Which processes are responsible for the differences?

2 Data and method

The focus of this study is to investigate the effects that subsurface flow has on ground temperature and moisture in the active 85 layer of a hillslope system located in a continuous permafrost environment. For this problem, the main governing processes which are relevant to consider are surface energy balances stemming from solar radiation, thermal insulation due to snow cover, sources of precipitation (snow, rain) with associated snow and/or ice accumulation, surface ponding and runoff on frozen or saturated ground, surface-subsurface infiltration in thawed and unsaturated ground, and subsurface water flow and heat transport in partially saturated, partially frozen ground. These processes are intricately coupled, in essence because water flow both above and below ground carries energy as a form of advective heat transport, and heat transport impacts the phase 90 state of water, as liquid, ice or ~~vapour~~vapor, which in turn exerts control on water flow and heat conduction.

A numerical model is configured to correspond to site-specific conditions representative of hillslopes in Adventdalen, Svalbard, which is driven by atmospheric forcing and landscape data measured on-site. ~~Even though site specific data was chosen~~

to run the model, the aim of this paper is to provide a general idea of processes governing hydro-thermal responses of the active layer to groundwater flow while accounting for the full complexity of realistic boundary conditions.

95 The model used is the Advanced Terrestrial Simulator (ATS v0.88, Coon et al., 2019). ATS is an open source, physically-based numerical model for coupled surface/subsurface thermal hydrology, specifically adopted for cold regions and permafrost applications (Painter et al., 2016).

A brief summary of the governing processes follows; for a full description see the cited references. ATS solves coupled conservation equations for energy and water mass transport, considering both above and below ground processes, based on

100 a multiphysics framework (Coon et al., 2016). (Painter, 2011) (Painter, 2011; Coon et al., 2016). The available energy at the surface-subsurface interface drives subsurface heat transport, and is obtained by solving for a surface energy balance equation (Atchley et al., 2015). Snow and ice on the surface affect heat conduction by reducing or increasing thermal conductivity, and subsequently impact heat transfer to the subsurface. Snow and ice are also subject to melting and ponding and can provide a source of water infiltration and/or surface runoff. Unfrozen water flow on the surface follows the Manning equation
105 Painter et al. (2016)(Painter et al., 2016).

In the subsurface, conductive heat transport follows Fourier's law, with an effective thermal conductivity based on the material properties and accounting for the phase state of the pore-filling fluid (as ice, liquid or air) (Painter, 2011). Advective heat transport occurs as heat carried by water movement in the porous media. Subsurface flow of water is governed by the extended Darcy law for partially saturated flow, where phase transitions follow the Clausius-Clapeyron relationship accounting for latent

110 heat transfer. Soil moisture retention curves, adopting a van Genuchten formulation, are used to describe effective permeability in the variably saturated pore space, accounting for the presence of air and ice, where ice is considered an immobile phase, causing a reduction in available porosity (Painter and Karra, 2014). Volume change for the phase changes between liquid and ice is accounted for by a pore compressible factor. Furthermore, ATS adopts a flux-conserving finite volume solution scheme and supports unstructured meshes, thus can conveniently be used for applications in 1D, 2D and 3D, accounting for vertical
115 and lateral processes in all dimensions considered.

2.1 Field data

Svalbard is located at 78°N and 15°E and therefore represents high-Arctic climate. Active layer thickness in Adventdalen has

increased with a rate of 0.7 cm yr^{-1} over the last decades and currently ranges between 0.9 and 1.1 m (Strand et al., 2020).

The observational weather data to drive the model (hereinafter referred to as the forcing dataset) is derived from a automatic weather

120 station located in Adventdalen (78.2°N 15.87°E). The station is operated by the University Center in Svalbard and captures all data needed for the daily surface energy balance, except for precipitation, in the time from 2013 to 2019. Precipitation data was retrieved from the long-term weather station at Longyearbyen airport (9 km west of the Adventdalen weather station; 78.24°N
15.51°E) operated by the Norwegian Meteorological Institute. Mean values for every day of the year (day-of-year average)

125 between 2013 and 2019 were calculated to represent current average weather conditions. Further data processing involved the classification of precipitation as rain if mean daily air temperatures were above 0° C and as snow if air temperatures were below

0° C. An adjustment for precipitation undercatch in Svalbard has been suggested to be 1.85 for snow and 1.15 for rain (Førland

Table 1. Physical properties of the subsurface material. Notations S_{uf} and D_{uf} denote saturated, unfrozen and dry, unfrozen conditions.

Material Property	Unit	Value
Porosity	$\text{m}^3 \text{ m}^{-3}$	0.4
Permeability	m^2	2×10^{-13}
Density	kg m^{-3}	2650
Van Genuchten α	Pa^{-1}	8×10^{-4}
Van Genuchten m	-	0.2
Thermal conductivity S_{uf}	$\text{W m}^{-1} \text{ K}^{-1}$	1.7
Thermal conductivity D_{uf}	$\text{W m}^{-1} \text{ K}^{-1}$	0.29 0.27
Specific heat capacity	$\text{J kg}^{-1} \text{ K}^{-1}$	850

and Hanssen-Bauer, 2000). Precipitation is multiplied by these factors. The resulting average yearly sum of rain (160 mm) and snow (170 mm w.e., total precipitation = 330 mm) for the period 2013–2019 was then redistributed to equal daily amounts during the rain- and snow period, respectively. The mean annual air temperature for the calculated averages is -2.8°C . A

130 representation of all variables within in the forcing dataset can be found in the supplementary material (Fig. S1). To inform the model, the same forcing dataset is used for the entire model domain (50 m transect length) without accounting for temperature lapse rates between the lower and upper part of the transect.

2.2 Simulation configurations

Three idealized model cases are considered; a steep case a steep case with a 22° inclination, a moderate case with a slope, a medium case with a 11° inclination slope, and a flat case with a 0° inclination slope. The flat case is used primarily as reference to evaluate effects of inclination and to normalise normalize quantities for analysis. The model cases are identical in all respects other than inclination. Note that the elevation difference between the uppermost and lowermost part of the slopes is 10 and 20 m for the medium and steep slope, respectively, but temperature does not change depending on altitude in this setup.

The inclinations are based on slopes as they can be found in Adventdalen and its southern tributaries mostly below 200 m elevation. Geologically, the slopes are located within the Carolinefjellet formation, which mainly consists of shale, siltstone and sandstone (Norwegian polar institute). All hillslope areas greater than 105° inclination in the area of question are shown in Fig. 1–a and b. An aerial image of the area is shown in panel c. In the same way as in panel a and b, slopes have been calculated in regions around the Arctic to evaluate how representative the slopes considered in this study are for the Arctic as a whole (Fig. 1d). It can be seen that even though great parts of the landscape are rather flat ($< 5^\circ$: 40–84%), all regions also have slopes in both categories (5 – 15° : 12–30% and 15 – 25° : 2–14%) or even steeper ($> 25^\circ$: 1–19%). For information on the methodology used to derive information about slope inclinations around the Arctic and for the values of the pie charts please see section 1 and Table S1 in the supplementary material.

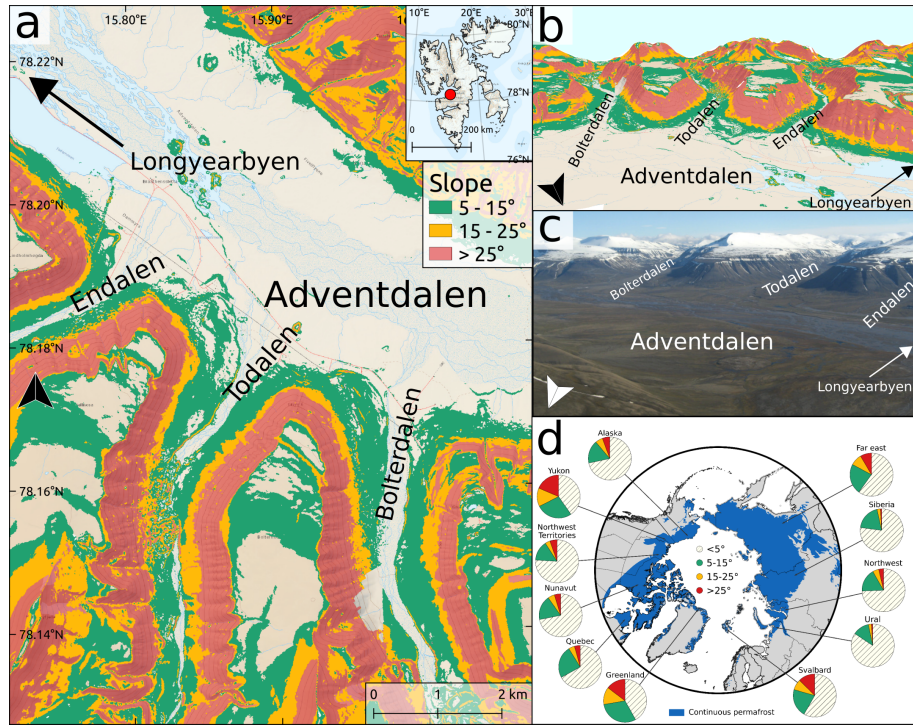


Figure 1. Overview over the general study area. (a) Map a shows a map with slope inclinations greater than 105° along some of Adventdalen's southern tributaries (Endalen, Todalen, Bolterdalen). (b) b: 3D view of the valleys and slope of the map in panel (a). Basemap data has been retrieved from the Norwegian polar institute. Inclination values are based on elevations from the Arctic DEM (10 m resolution; Porter et al., 2018). (c) Areal c shows an aerial image of Adventdalen overlooking the same area as in the maps in panels (a) and (b). The picture was taken from a helicopter by A. Skosglund (Norwegian polar institute). d: Overview over slopes in Arctic continuous permafrost regions based on different administrative areas following the classification in panels a and b.

The flat control case corresponds to areas with no considerable inclination as they can be found in the valley bottom in Adventdalen. These areas are characterized by holocene glaci-fluvial deposits (Norwegian polar institute). It can be seen that some slopes end in the tributaries of Adventdalen (Endalen, Todalen, Bolterdalen), which contain seasonal river systems. Other, mainly north facing, slopes do not necessarily end in a surface water body but somewhere in the flat part of the Adventdalen valley bottom. This is important for the choice of boundary conditions in the model domain.

2.2.1 Model domain and boundary conditions

To represent the slopes in ATS, each case has its own mesh. The slope-meshes consist of a sloped part ($x = 0-50$ m) with a constant slope of 11 and 22° , and an adjacent flat valley bottom ($x = 50-66$ m). Each model case has a corresponding surface and subsurface mesh. The surface mesh is a 2D layer which extends 5066 m in x -direction and 1 m in y -direction, and the subsurface mesh extends 5066 m in x -direction, 1 m in y -direction and 20 m in the z -direction (Fig. 2). Both have a lateral

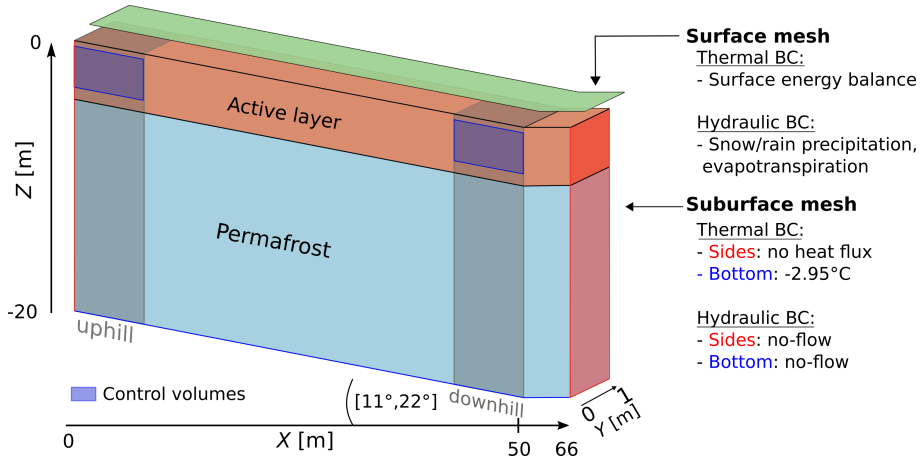


Figure 2. Conceptual representation of the surface and subsurface modeling domain. Shaded grey areas on either side of the transect indicate the uphill and downhill observation locations, red indicates the sides of the model, blue boxes represent the control volumes (CV) and a blue line at the bottom indicates the bottom boundary. Thermal-hydraulic boundary conditions (BC) on the surface, sides and bottom are listed on the right.

resolution of 2 m yielding 25–33 mesh elements along the x -direction. Only one element with unit width is assigned in the transverse y -direction. Thus, the subsurface elements are 3D volumes and yield volumetric flow quantities, but the model setup effectively represents a 2D transect of the surface-subsurface system with unit width (for actual mesh representations please refer to Figure S2 in the supplementary material). This approach has found to be a valid simplification of complex slope systems (Jafarov et al., 2018; Jan and Painter, 2020). In the uppermost meter of each column, cells are generated with a higher resolution of 0.05 m height in the vertical direction, in order to improve the spatial resolution of the active layer. With increasing depth, cell thickness gradually increases.

The downhill end of the transect represents the valley bottom, and allows for water accumulation and potential ponding on the surface. All cases assume a homogeneous material throughout the model domain consistent with mineral soils typically encountered in the area (Schuh et al., 2017). We do not consider an organic layer in our setup as they are absent on most parts of the slopes in the Adventdalen area. The physical and material properties used to describe the subsurface domain (Table 1) are consistent with a previous study based on the UNISCALM site in Adventdalen (78.2°N 15.75°E), which showed good agreement with subsurface measurements and produced realistic active layer depths (Schuh et al., 2017).

Figure 2 depicts the model domain and the respective defined points and faces of interest. The domain boundaries in the subsurface. The boundary conditions for the subsurface domain are prescribed as no-flow boundaries on the right, left and bottom left and right side, and at the bottom. Therefore, the uphill end conceptually represents a water divide, as no flow enters the domain from further up. The downhill end of the transect represents the valley bottom, and allows for water accumulation and potential ponding on the surface. The right-most boundary reflects a symmetry boundary, representing a simplified U-shaped valley bottom. This valley bottom ($x = 50$ –66 m) is needed to avoid edge/boundary effects and is omitted

in the analysis of the results. Given the length of the domain in x -direction (66 m), this would be a very short slope system, but serves the purpose of a generic slope and provides a reasonable trade off between model resolution and computational time. The bottom temperature is set to -2.95°C , which has found to be the temperature at 19 m depth in a borehole in Endalen, one of Adventdalen's tributaries (Hanssen-Bauer et al., 2018). The borehole is located on a slope and therefore assumed to be representative for other slopes in Adventdalen. As the borehole temperature experiences a linear increasing trend throughout the 2013–2019 period, the mean value of the same period is used. The surface is subject to hydro-meteorological conditions measured on-site (the forcing dataset), which effectively drives the dynamics of heat and water flow through the model system. Precipitation is added as snow and rain on the surface, which allows for infiltration, and heat is supplied by the surface energy balance. Water can leave the system via evapotranspiration evaporation and the surface allows for snow and ice accumulation as well as water ponding. Snow distribution is intentionally for these simulations has intentionally been disabled, in order to yield the same snow accumulation on the surface of the model domain. This is due to the fact that an accumulation of all available snow on the downhill side of the slope is not realistic and the fact that this would considerably increase the complexity of our analysis and the disentanglement of the effects of groundwater flow on the hydrothermal state of the active layer, which is the focus of this study.

The model output is given as field-cell values in selected locations cells of the sloped part of the model domain. Analysis of field-these values includes temperature, saturation and thermal conductivity, and heat capacity, extracted at 0.1 m, 0.2 m, 0.40.5 m and 0.751 m depth at an uphill and downhill location of each model domain. These depths are chosen as they represent the near-surface soil conditions, the middle of the active layer and the bottom of the active layer. Temperature differences over the entire transect are extracted for specific points in time.

For analysis of fluxes, two control volumes (CV) are defined, also located uphill and downhill (see Fig. 2). The uphill CV extends from 0 to 2 m in x -direction, 0 to 1 m in y -direction, and from 0.1 to 0.6-0.1 to -0.6 m in z -direction. The volume of the box is thus approximately $\sim 1 \text{ m}^3$. The downhill CV is defined as a box from 48 to 50 m in x -direction, 0 to 1 m in y -direction, and 0.1 to 0.6-0.1 to -0.6 m in z -direction ($\sim 1 \text{ m}^3$). Since the left and right boundary are no-flow boundaries, lateral fluxes in the CVs are only represented on the right boundary of the uphill CV and on the left boundary of the downhill CV. We placed the CVs at these locations to capture the most extreme values within the domain and to link them to the cell values in the first and last column. The upper boundary is moved 0.1 m below the surface, as the surface itself includes more processes than subsurface faces, which would complicate the comparison to the bottom-boundary face of the CV. Each face of the box is used to capture advected and diffusive energy flux, and mass flux into and out of the domain during the simulation. Lateral fluxes in the CVs are only represented on the right boundary of the uphill CV (flux directed outward) and on the left boundary of the downhill CV (flux directed inward). We placed the CVs at these locations to capture the most extreme values within the sloped part of the domain and to link them to the cell values in the same locations.

2.2.2 Model initialization and spin-up

Model initialisation and spin-up is conducted with a 3-step procedure following previously established routines for permafrost-hydrological modelling (Frampton et al., 2013; Karra et al., 2014; Painter et al., 2016). First, a single 1D column

is used to establish hydrostatic conditions with the water table at a target depth, using pressure boundary conditions for the top and bottom faces of the model. Second, the soil and water in the column is cooled from below with an assigned sub-zero bottom temperature, until the column is fully frozen and reaches a cryotic steady-state. In the third step, the forcing dataset is used to bring the thermal hydraulic conditions of the column model into an annual steady state. The day-of-year average 215 yearly cycle created from the weather data is repeated for 50 years to create the forcing dataset. After 50 years, this yields an inter-annual temperature differences throughout the column of less than 0.01°C.

This above procedure is necessary to obtain a physically consistent system which can be used as initial condition for main simulation runs. The resulting state from this 1D single column spinup model is mapped to each of the 25–33 columns of the hillslope transect model. Thereafter, the main model runs are conducted by using the forcing dataset once again, this time 220 allowing for all lateral and vertical dynamic processes.

This final fourth step is run for 100 years, until an annually periodic steady-state for the full surface-subsurface hillslope models is obtained. This results in a representation of the hydrothermal state of the subsurface corresponding to the current 2013–2019 average weather conditions. The process is repeated for each of the three model inclination cases to ensure effects of hillslope inclination are embedded in the final model results.

225 3 Results and discussion

3.1 Temporal analysis of ground temperatures

Daily ground temperatures in the active layer (0.1 m, 0.2 m and 0.40.5 m depth) and near the permafrost table (0.751 m depth) vary between the different inclination cases, and there are also temperature differences between the uphill and downhill observation locations. Additionally, timing of thaw and freeze-up varies between cases. To enable a systematic study of the impact 230 of the different hillslope inclinations, we consider daily temperature differences ΔT_I between the steep slope and flat case (steep-flat), as well as between the medium slope and flat case (medium-flat). We also consider daily temperature differences ΔT_E between uphill and downhill observation points (uphill-downhill), corresponding to different elevations along a hillslope (Fig. 3). [A time series of daily subsurface temperatures in each depth and location can be found in Fig. S3 in the supplementary information.](#)

235 There is ~~significant~~-variability in these temperature differences over the year, with most pronounced differences occurring during the warm season, typically including a peak ~~at onset of thaw just after the thaw period~~ and another peak ~~before~~ ~~after~~ freeze-up, indicating greatest differences occurring during these times. Between the uphill and downhill side in the steep and medium slope (Figures 3a,b), it can be seen that the uphill side is warmer than the downhill side throughout the year (positive ΔT_E), with two short exceptions ~~during thaw and just after thaw and after~~ freeze-up (negative ΔT_E). The warming is strongest 240 in summer ~~with two peaks developing just after thaw and before freeze-up. The warming and~~ occurs first close to the surface (0.1 m, orange line) exhibiting a temporal lag effect with depth. At 0.751 m depth (yellow) the warming effect is delayed and smaller due to the overall colder temperatures near the permafrost table. ~~The Just after freeze-up, however, differences at 1 m depth are largest as cooling close to the permafrost table occurs faster than the the rest of the active layer due to the presence of~~

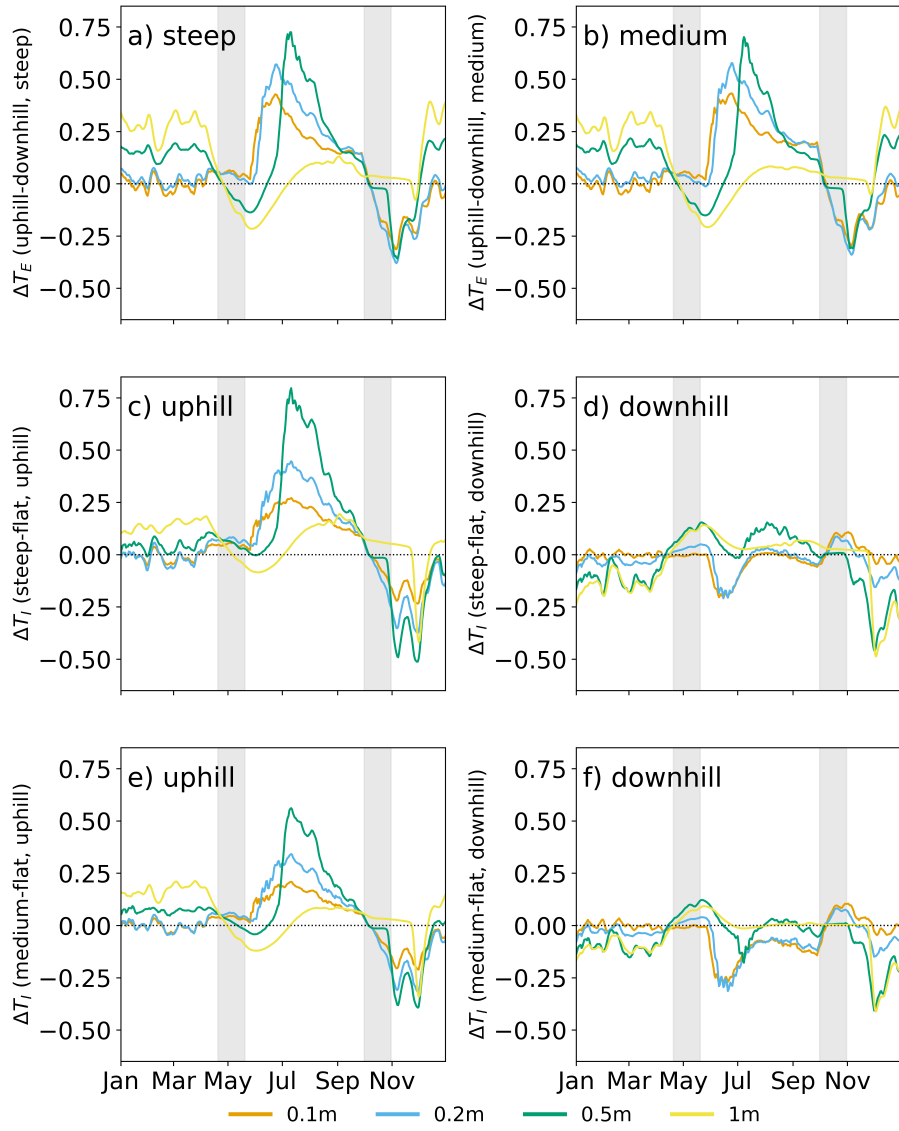


Figure 3. Daily temperature differences (averaged over a 7-day window) ΔT_E (a, b) and ΔT_I (c, d, e, f) in four different depths within the active layer. Grey shaded areas indicate periods of thaw and freeze-up. Temperature differences between locations (ΔT_E) are calculated by subtracting the downhill temperature from the uphill temperature. Resulting positive values indicate warmer temperatures uphill, while negative values indicate colder temperatures. Temperature differences between slopes (ΔT_I) are calculated by subtracting the flat case temperatures from each sloped case (steep and medium). Positive values indicate that the slopes are warmer, while negative values imply that the slopes are colder compared to the flat case.

the permafrost. The overall greatest temperature differences can be seen near the surface (0.1m in the middle of the active layer 245 (0.5 m depth) at the onset of freeze-up around July in the steep case (~ 1.2 to 0.8°C warmer than downhill).

Temperature differences ΔT_1 between the steep slope and the flat case (Fig. 3c,d) and between the medium slope and the flat case (Fig. 3e,f) show that on the uphill side, the slopes are warmer in summer, colder ~~during after~~ freeze-up and very similar to the flat case in winter. On the downhill side, the slopes ~~are slightly, are~~ colder than the flat case in winter ~~and significantly colder during summer and just after thaw and~~ after freeze-up. ~~During freeze-up however, the downhill sides are slightly warmer than the flat reference case.~~

250 This is especially true for the medium slope and near-surface temperatures. Deeper layers are have similar temperatures as the flat case or are even slightly warmer. An overview of the yearly maximum differences is given in Tables ?? and ?? . The greatest temperature difference between uphill and downhill observation points occurs at 0.1 m depth ($\Delta T_E=1.18^\circ\text{C}$) for the simulation case with steep slope inclination (Table ??). Also, the steep slope case exhibits greater differences than the medium slope case for all depths in the active layer. Note however that the differences for the steep slope case are not quite double that of the medium slope case, despite the inclination being doubled.

255 Considering the temperature difference between slope inclination cases (Table ??), the greatest difference occurs when comparing the steep and flat cases, at 0.1 m depth on the downhill side (temperature differences $\Delta T_1=1.06^\circ\text{C}$). This indicates the importance of near-surface processes in summer on the downhill side. On the uphill side, the largest difference is visible at 0.4 m depth ($\Delta T_1=0.55^\circ\text{C}$). This inversion of temperature difference indicates that different processes are responsible for these differences in subsurface temperatures at various depths ~~E~~ is given in Tables S2 and S3 in the supplementary material.

260 Maximum temperature difference between uphill and downhill observation sides (ΔT_E) at several depths within the active layer for each hillslope case; positive values indicate warmer temperatures occur uphill (steep or medium) compared to downhill. ΔT_E 0.1m 0.4m 0.8m 10m steep 1.18 1.01 0.80 0.87 medium 0.56 0.71 0.69 0.52

265 Maximum temperature difference between various hillslope inclination cases (ΔT_1) at several depths within the active layer; positive values indicate warmer temperatures occur in the sloped (steep or medium) cases compared to the flat case. 0.1m 0.2m 0.4m 0.75m 0.1m 0.2m 0.4m 0.75m steep flat 0.24 0.37 0.55 0.21 1.06 0.88 0.79 1.00 medium flat 0.14 0.22 0.32 0.11 -0.52 -0.57 -0.51 -0.59

3.2 Spatial analysis of ground temperatures

270 The greatest ~~difference in temperature~~ temperature difference along the subsurface transect ~~is occurs~~ between the two outermost ~~columns~~ slope locations (at $x=0\text{ m}$ and $x=50\text{ m}$), corresponding to the two locations farthest apart along the hillslope. To better ~~visualise~~ ~~visualize~~ the ground temperature differences between cases throughout the subsurface domain, the temperature difference between the steep and the flat case (Fig 4a), and the medium and flat case (Fig 4b) in the upper 1.2 m of the subsurface are considered. Note that Fig 4 shows cell-based temperature differences between cases; thus slope inclination is not depicted.

275 The upper three ~~panels in each figure~~ plots in each panel (a and b) show snapshots of temperature differences during thaw (June) and summer (July, August), and the lower three ~~panels~~ plots show temperature differences during freeze-up (October, November) and winter (December). In both cases, the dates are separated by 20 days. For each day, the 0°C isotherm(s) from the steep and medium case respectively is (are) represented as black dotted line(s). ~~During thaw they represent the maximum depth at which temperatures exceed 0°C (i.e. the soil above is unfrozen, the soil below is frozen) and during freeze-up, they~~

Table 2. Average temperature of the entire transect up to 1.2 m depth for each day of the snapshots.

	average temperature [°C]					
	Jun 30	Jul 20	Aug 9	Oct 28	Nov 27	Dec 7
steep	0.73	1.76-1.72	2.02	-0.76-0.7	-0.95-0.85	-5.72-5.14
medium	0.65	1.61-1.6	1.92-1.9	-0.74-0.68	-0.92-0.82	-5.67-5.1
flat	0.64-0.56	1.56-1.47	1.82-1.79	-0.73-0.64	-0.87-0.78	-5.64-5.06

280 show unfrozen parts of the subsurface (i.e. the soil between the lines is unfrozen, the soil outside is frozen). The average temperature in this volume of the subsurface (upper 1.2 m) is given in Table 2.

Ground temperatures in the sloped cases are generally warmer than in the flat case during thaw and summer (red shades). The temperature differences are greatest near the progressing thaw front, i.e. near the 0 °C isotherm, as well as on the uphill side ($x=0$ m), but a gradual change towards same similar temperatures as the flat case (red to white) can be observed in the 285 lateral direction (increasing x). Note also the last column on the downhill side ($x=50$ m) exhibits colder temperatures than the flat case (blue shades) during this time period. The temperatures below the permafrost table (at approximately 0.81 m depth) are only slightly warmer in the steep case, and essentially unchanged in the medium case, for the summer snapshots.

290 During freeze-up (October 28 and November 17 snapshots) the sloped cases are generally colder in the topsoil and warmer in the permafrost compared to the flat case. By winter (December 7) almost the entire 1.2 m depth of the steep slope becomes colder than the flat case (light blue), with the last column being. Only some areas on the downhill half of the transect remain slightly warmer (yet below freezing) than the flat case, while the very last column of the slope is significantly colder (dark blue). The medium slope case still has a small region in the uphill part of the domain close to the permafrost table that remains warmer than the flat case.

295 The 0 °C isotherms show that on June 30/July 20, the steep slope already develops a deeper thawing front in the first 20 m of the transect compared to the medium/flat slope. On July 20/August 9, the steep slope is warmer throughout most of the active layer thickness (approx. 0.81 m) of the transect; only the last few meters of the domain ($x=45-50$ m) exhibit equal or cooler temperatures than column shows similar near-surface temperatures as in the flat case.

300 In the medium slope case, only the first 10 the first 35 to 40 m ($x=0-100-35/40$ m) of the slope show warmer temperatures in the active layer on that day and deeper progressing thaw fronts on all dates, compared to the rest of the slope. In both cases, it can. The last 10 to 15 m ($x=35/40-50$ m) exhibit shallower thaw fronts. In both, the October and November snapshots, the freeze-up process shows how the transects freezes from top to bottom, as well as slowly from the permafrost table upwards, thereby exhibiting two-sided freezing. Between October 28 and November 18 it can therefore be seen that even though the ground appears to be frozen from the surface, it is still unfrozen in the lower part of the active layer. By December 7, the last column ($x=50$ m) remains significantly cooler than the rest of the slope, causing the active layer to be shallower the entire active layer is frozen.

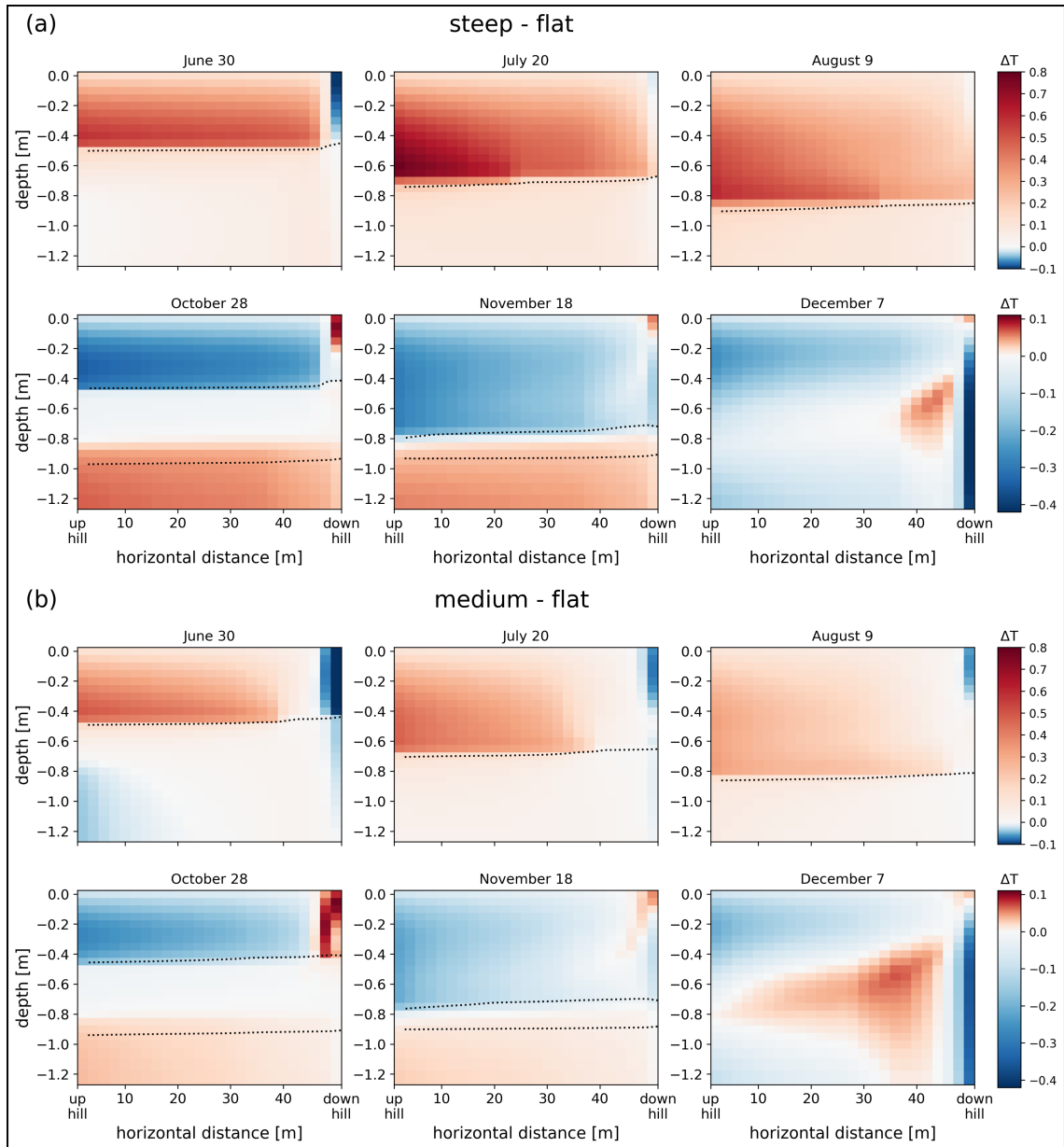


Figure 4. Temperature difference between (a) a the steep and the flat case and (b) b the medium and flat case at six selected dates highlighting thaw, summer, freeze-up and winter. Red colors indicate warmer temperatures in the hillslope cases than in the flat case, blue colors indicate cooler temperatures (note the color scale differs between summer and winter comparisons). The black dotted line indicates the 0°C isotherm(s) in the corresponding hillslope case at the respective dates. During freeze-up, it can be seen that two-sided freezing occurs. The figure only shows the upper 1.2 m of the entire simulation domain extends to 20 m below the surface.

To highlight differences in the developing thaw depth between cases, spatially averaged thaw depths over the entire transect for each case are calculated (Fig. 5a). As noted above, the steep slope ~~has experiences~~ a warming effect on the uphill section of the transect, which causes its maximum thaw depth (Fig. 5a, dark blue line) to be greater; ~~the~~ spatial mean active layer depth on the date of maximum active layer depth is ~~-0.77~~^{1.03} m. On the other hand, the medium-slope (cyan line) does not develop a substantially deeper maximum active layer thickness than the flat case, as the temperature difference is not enough to increase it (~~-0.73~~^{min.:1.03} m maximum thaw depth in both cases). However, it can be seen that the medium-slope case reaches maximum active layer thickness slightly earlier than the flat case (yellow) and freezes up slower, reflecting the slightly warmer temperatures.

Representation of thaw depth compared between the steep (blue), medium (cyan) and flat case (yellow). (a) shows daily, 310 spatially averaged thaw depth averaged over a 5-day window from May to December in the last year of the simulation. Note that thaw depth is defined as cells within the model domain that exceed 0°C . (b) shows snapshots of the developing thaw depth throughout the transect (defined as the 0°C isotherm, vertically interpolated). Solid, dashed and dotted lines represent the three chosen points in time July 20, September 18, and November 18, respectively.

Three snapshots of the thaw progression throughout the subsurface during the summer and freeze-up seasons are shown 320 in Fig. 5b. The steep slope case (dark blue) has the deepest thaw depth in July throughout most of the transect (max. -0.6 m), between $x=0$ –⁴⁵₄₅ m, ~~max.: 1.03 m~~, while the medium case (cyan) has a similar thaw depth (max. -0.58 m) as the flat case (yellow, max. -0.55 m) for lateral distances between $x=10$ –⁴⁸₄₈ m (5b, solid lines). Between $x=0$ to 10 m the thaw depth in the medium case in July is deeper and the last two meters ($x=48$ to 50 m) shows a shallower thaw depth as compared to the flat case. This observation on thaw depths for July 20 is consistent with the previously discussed temperature differences in Figure 4; 325 temperatures are generally warmer uphill and cooler downhill for the sloped cases, and the cooling effect is primarily observed within the last few meters of the domain.

On along the transect). The medium slope (cyan line) exhibits a smaller uphill warming than the steep slope resulting in a spatial mean active layer depth on the date of maximum thaw depth, corresponding to the active layer thickness (September 18, dashed lines), the steep case shows the deepest active layer (max. ~~0.81~~^{active layer depth of 0.986 m} (min. ~~0.975~~^{0.975} m, 330 ~~max.:1.030 m~~), while the medium case along the transect), which is only slightly deeper than in the flat case (max. -0.77 m and ~~0.75~~^{0.975} m, respectively). Both slopes show a shallower active layer in the last few meters of the transect ($x=45$ to 50 m). This again is consistent with the previously discussed temperature differences, where generally significantly cooler temperatures are observed on the downhill side than on the uphill side (ΔT_E) and the slopes being colder than the flat case (ΔT_F yellow line).

During freeze-up on November 17 (dotted lines), the flat case has attained a fully frozen active layer. The sloped cases however still exhibit unfrozen patches of soil ("thaw bulbs") between 0.6 and 0.8 m depth. This indicates that the temperature changes caused by slope inclination, specifically warmer temperatures in the uphill-center sections of the transect, creates a delay in freeze-up especially towards the center-downhill sections of the domain. However, the previously warmest parts of the sloped cases during summer are already frozen at this time, which is related to latent heat consumption differences in the 340 different parts of the transect.

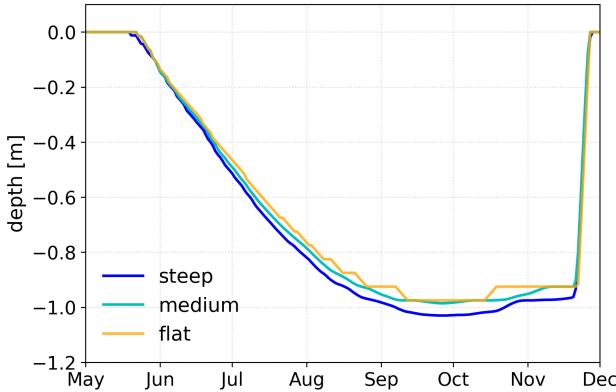


Figure 5. Representation of thaw depth compared between the steep (blue), medium (cyan) and flat case (yellow) as daily, spatially averaged thaw depth (averaged over a 5-day window) from May to December in the last year of the simulation. Note that thaw depth is defined as cells within the model domain that exceed 0°C .

A further observation is that two-sided freezing occurs. This is evident by the remaining thaw bulb with encroaching freezing front both from above as well as below (dotted lines). Subsequently, the active layer is fully frozen again on November 20 for the steep slope case, on November 19 for the medium slope case, and finally on November 18 for the flat case.

In summary Overall, we observe that the steep slope case has a notable influence on thaw propagation and active layer thickness, which we attribute to an increase in ground temperatures compared to the flat case, observed primarily in the center-uphill side of the subsurface during most of the summer period. The warming effect in the medium slope case is not sufficiently strong to increase the active layer in most of the transect. The medium sloped case only shows a marginal increase in maximum thaw depth, but it can be seen that both slopes start thawing earlier and the day of maximum thaw depth is reached earlier compared to the flat case. This results in a active layer thickness of 0.81 m, 0.77 m and 0.75 m for the steep, medium and flat case respectively. However, the warming effect for the medium slope causes maximum thaw depth to be reached earlier and freeze-up to be delayed. This can be seen by integrating the total volume of unfrozen soil over the warm season (defined as days with at least one unfrozen cell in the subsurface model domain, here resulting in May 16 to November 20; 187 days to October 2; 140 days). The steep slope amounts to a total volume of 22972936 m³ (or an average of 12.320.97 m³ per day), the medium slope amounts to 22022905 m³ (average 11.820.75 m³ per day), and the flat slope amounts to 21752885 m³ (average of 11.620.61 m³ per day). This indicates that the slopes in general have a greater unfrozen volume of soil, even though the active layer is not necessarily deeper active layer depth in the medium slope case is not substantially different. Hence, the warming effect due to slope inclination does not only play a role in the vertical soil profile, but also in the timing of freeze and thaw.

360 3.3 Saturation and thermal conductivity and heat capacity

Due to lateral gravitational water flow during the warm period, moisture gets drained from the uphill side and accumulates on the downhill side, and yields. This yields lower liquid saturation in the uphill section and greater liquid saturation there in the downhill section when compared against the flat reference case which is not subject to lateral flow (Fig. 6, first column). This leads subsequently to greater ice saturation on the downhill side differences in ice saturation during the frozen period (Fig. 6 second column). The Notably, there is little difference in saturation between the medium and steep slope. In fact, the medium slope is slightly more saturated on the downhill side compared to the steep case. This is likely due to the geometry of the slopes and subsequent valley bottom. The reduced/increased ice and liquid saturation in the slopes, and consequently increased/reduced air saturation (Fig. 6 third column), results in a considerably lower/greater effective thermal conductivity during winter and slightly lower/greater effective thermal conductivity during summer in the uphill and downhill section, respectively (Fig. 6 fourth column). Considering the little snow cover in winter (max. 0.01 m, see Fig. S2S4), the effect should be an enhanced heat loss (cooling of the ground) during winter, and slightly enhanced heat gain (warming of ground) during summer, when compared against the flat reference case.

Daily values for liquid, ice, and air saturation (columns 1–3) and thermal conductivity (column 4) at 0.1, 0.2, 0.4 and 0.75 m depth (rows 1–4). Colors represent the three different cases and solid and dashed lines mark uphill and downhill sides, respectively. The horizontal dashed lines in the saturation plots indicate 100% saturation. The vertical dashed lines mark the first and last day at which ground surface temperatures exceed 0°C

Recall the previous discussion on temperature differences between the sloped and flat cases. Furthermore, differences in liquid saturation change the bulk heat capacity (Fig. 3d,f). The downhill side of the sloped cases experience cooler winter temperatures, especially shortly after freeze-up in late November. This is consistent with the differences in effective thermal conductivity, as an increased thermal conductivity during cold periods enables an enhanced ground heat loss, yielding cooler winter ground temperatures. However, summer temperatures also exhibit significant cooling when compared to the flat case (Fig. 3d, f). This is not consistent with the increased effective thermal conductivity summertime, as it should enhance heat uptake to the ground, leading to warmer ground temperatures. Thus we conclude changes in effective thermal conductivity alone does not suffice to explain the temperature changes incurred on the downhill side two sections. While it is reduced in the uphill section, it is higher in the downhill section of the domain. This causes the uphill section to warm up and cool down faster than the downhill section and contribute to overall warmer temperatures uphill. Downhill, it slows the warming and cooling process down. A 2D representation of differences in heat capacity between the steep and flat and the medium and flat case throughout the upper 1.2 m of the domain for the two hillslope cases can be found in Fig. S5 in the supplementary information (analogous to Fig. 4).

390 Next, consider

Recall the previous discussion on temperature differences between the sloped and flat cases on the uphill side of the domain for the hillslope cases (Fig. 3c,e). They are slightly drier at depths 0.2 m, 0.40.5 m and 0.751 m, both for summer with less liquid saturation, and winter with less ice saturation (Fig. 6, first and second columns, respectively). This slightly reduces effective

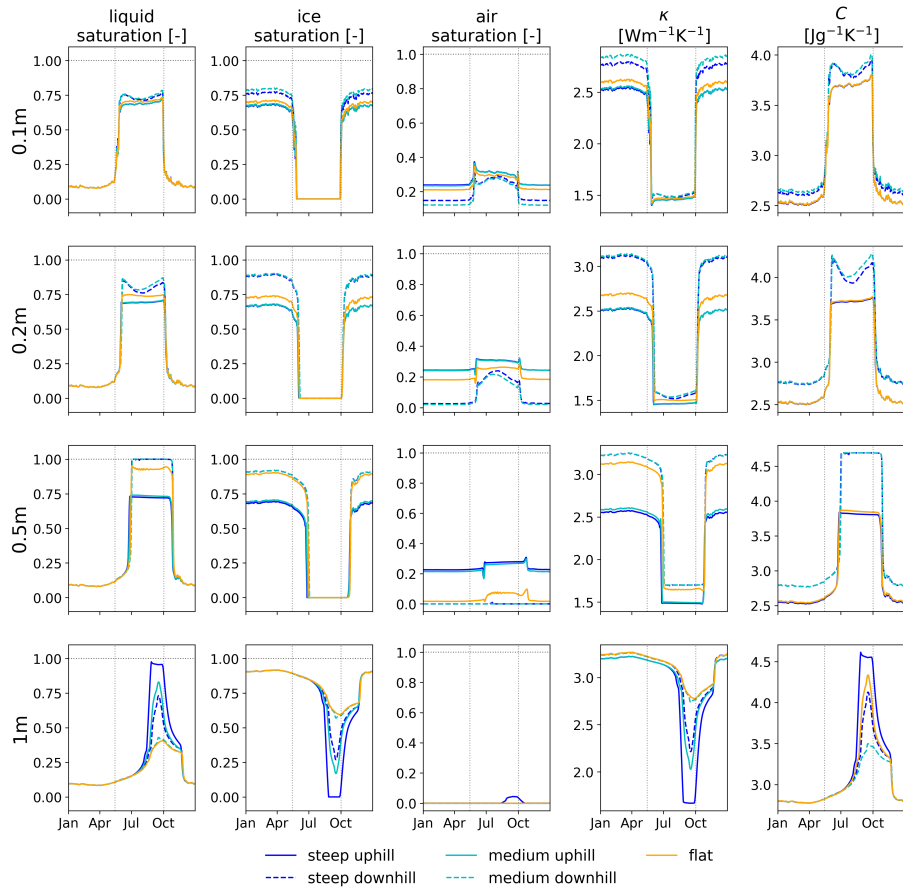


Figure 6. Daily values for liquid, ice, and air saturation (columns 1–3), thermal conductivity (κ ; column 4) and heat capacity (C ; column 5) at 0.1, 0.2, 0.5 and 1 m depth (rows 1–4). Colors represent the three different cases and solid and dashed lines mark uphill and downhill sides, respectively. The horizontal dashed lines in the saturation plots indicate 100% saturation. The vertical dashed lines mark the first and last day at which ground surface temperatures exceed 0°C.

thermal conductivity with respect to the flat case at those depths, mainly in winter and slightly discernible also in summer (Fig. 395 6, fourth column). Thus, when compared against the flat reference case, the uphill side of the inclined cases should exhibit warmer ground temperatures during winter due to reduced thermal conductivity (greater insulation) and hence reduced heat loss. During summer, the reduced thermal conductivity is only minor, but if anything may lead to a reduced heat gain, leading to slightly cooler ground when compared to the flat case. However, this is not entirely consistent with the previously observed temperature differences for the uphill side (see Figures 3c,e); while winter temperature differences are small between 400 the sloped and flat cases positive (after the freeze-up effect) and hence are consistent with smaller heat loss to the atmosphere than in the flat case, summer temperatures are warmer in the sloped cases, not cooler. The greatest difference for both slopes

can be found at 0.4 m depth, with smaller differences closer to the surface. During freeze-up, the uphill sides are cooler. This can partially be explained by reduced heat capacity in the uphill section, which allows for faster warming and overall higher temperatures. This effect potentially outweighs the reduced heat conduction from the atmosphere into the ground through lower thermal conductivity, but does not explain the entire difference.

Next, consider the downhill side (Fig. 3d,f). The sloped cases experience cooler winter temperatures, especially shortly after freeze-up in late November. This is consistent with the differences in effective thermal conductivity, as an increased thermal conductivity during cold periods enables an enhanced ground heat loss, yielding cooler winter ground temperatures. However, summer temperatures exhibit very similar or even cooler temperatures than the flat case (Fig. 3d, and especially in f). This is also apparent for not entirely consistent with the increased effective thermal conductivity summertime, as it should enhance heat uptake to the ground, leading to warmer ground temperatures. Thus, we conclude changes in effective thermal conductivity alone do not suffice to explain the negative temperature differences on the downhill side for the two hillslope cases in comparison to the flat case. Considering heat capacity, however, it can be expected that wetter soils in the downhill section require more heat to warm up and thus remain slightly colder, which can counteract the effect of thermal conductivity to the findings in Fig. 3d,f.

When only comparing the two observation locations uphill vs. downhill within the slopes (Fig. 3a,b), similar effects as previously described can be seen. Again, winter differences can be explained by increased heat loss to the atmosphere due to greater thermal conductivity on the downhill side, but summer differences cannot be explained by changes in saturation and effective thermal conductivity alone, but are partly attributable to lower heat capacity. However, these described effects are not sufficient to explain the full range of temperature difference.

In summary, moisture redistribution causes thermal conductivity to be greater downhill than uphill, causing changes to the effective thermal conductivity along the lateral transect for hillslopes. Although this impacts the diffusive mainly causes differences in thermal conductivity as well as heat capacity between the uphill and downhill section. Thermal conductivity is likely to affect lateral transport of energy (heat conduction) through the subsurface, summer ground temperatures cannot be linked directly to differences in effective thermal conductivity; this is further investigated by studying, but to better understand the effects of all the diffusive as well as advective energy transport on temperature differences, we investigate heat fluxes in several directions and at multiple locations in the transect in the next section.

3.4 Energy fluxes

Vertical and lateral energy fluxes are calculated through the faces of two control volumes in the subsurface domains; one placed on the uphill side and the other on the downhill side (see Fig. 2). The objective is to investigate fluxes within the active layer, hence the CVs extend from 0.4-0.1 m depth to 0.6-0.6 m depth below the surface. Daily flux values averaged over a 90-day window are considered, defined as positive if entering the CV, and negative if leaving the CV. Diffusive heat flux (energy transport by conduction) and advective heat flux (energy transport by water flow) obtained this way are shown in Figs. 7 and 8, respectively, for both the uphill CV (solid lines) and downhill CV (dashed lines). The central box (conceptually) aids the interpretation of the fluxes across corresponding faces of the control volume. Fluxes across the top and bottom faces represent

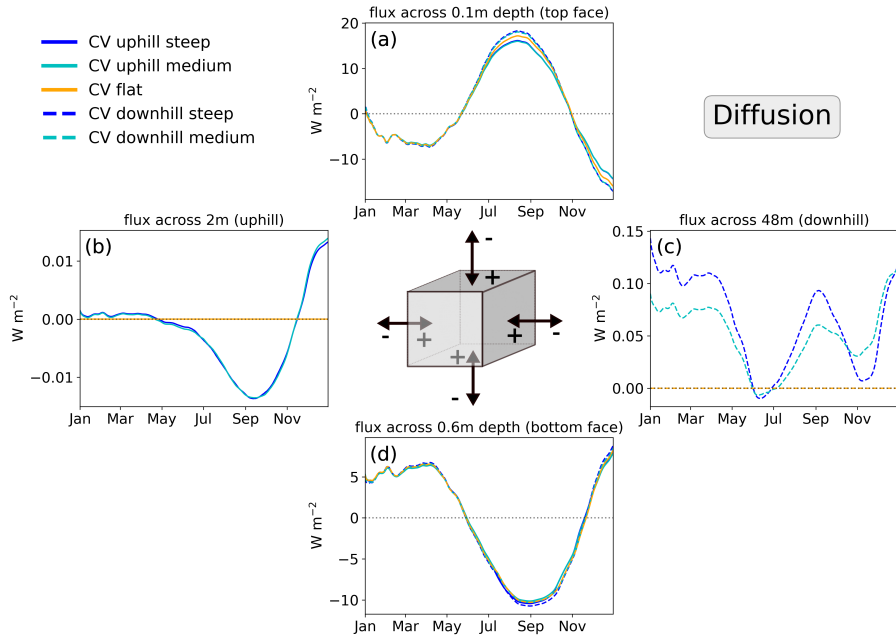


Figure 7. Daily values of diffusive heat flux on the faces of the control volume (CV; 7-day 90-day moving average) at the uphill (solid) and downhill (dashed) CV locations. Colors represent the steep (blue), medium (yellowcyan) and flat (greenyellow) case, respectively. The sign convention adopted is positive values represent heat entering the CV and negative values leaving the CV. Due to the definition of the CV boundaries, lateral fluxes only occur on the right face for CV up and on the left side for CV down.

fluxes at $z=0.1$ and $z=0.6$ m depth, while fluxes across the left and right faces represent fluxes across vertical faces at $x=48$ and $x=2$ m, respectively. The distance is given as distance from the left domain boundary ($x=0$ m). Note the lateral fluxes are only displayed on one of the vertical faces of the CVs due to their location on the domain boundaries, as the opposing sides ($x=50$ and $x=0$ m) are no-flow boundaries represent the edges of the slope. Fluxes can vary by more than one order of magnitude between cases, which results in different ranges of values for the vertical axes.

The most pronounced flux is vertical diffusion heat diffusion near the surface (-20 – 20 W m^{-2}), which shows little relative difference between the hillslope cases. Across the top face, i.e. at 0.1 m depth, the downhill CVs (Fig. 7a, dashed) show slightly greater heat gain through heat diffusion in summer (up to 5 – 2.5 W m^{-2}) and slightly greater heat loss during freeze-up, than the uphill CVs (solid). Winter diffusive heat fluxes are almost identical. Lateral heat diffusion is smaller, but more pronounced and quite variable in the downhill CVs (Fig. 7bc, dashed, -0.1 – 0.01 – 0.7 W m^{-2}). It is highest during just before freeze-up and in winter, which is due attributable to a high temperature gradient between the penultimate and the last column in the model slope domain.

In the uphill CV (Fig. 7eb, solid), the lateral heat diffusion is more than one order of magnitude smaller (-0.02 – 0.01 – 0.03 W m^{-2}) and heat is being lost in summer, but gained during after freeze-up in winter. This is also consistent with the

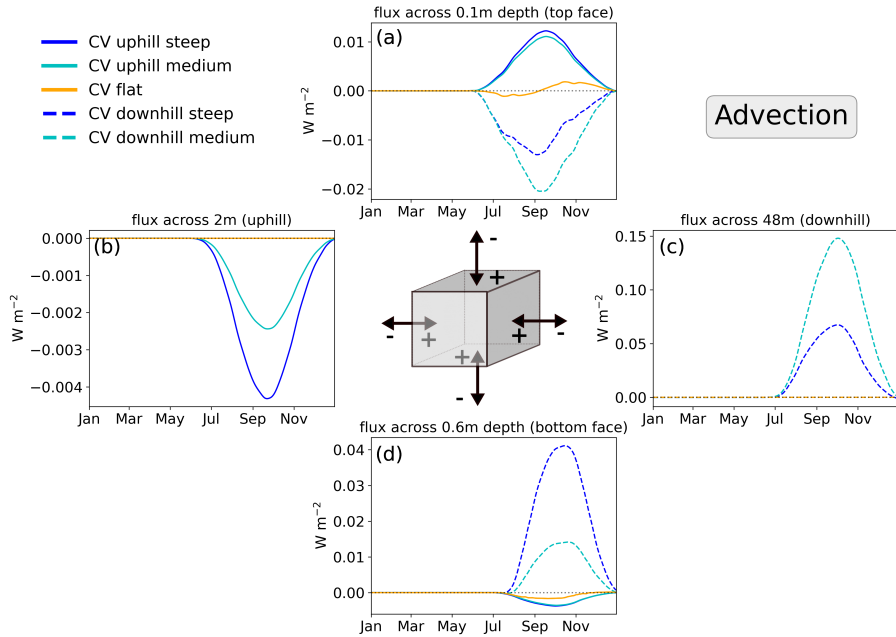


Figure 8. Daily values of advective heat flux on the faces of the control volume (CV; [7-day](#) [90-day](#) moving average) at the uphill (solid) and downhill (dashed) CV locations. Colors represent the steep (blue), medium ([yellow](#)[cyan](#)) and flat ([green](#)[yellow](#)) case, respectively. The sign convention adopted is positive values represent heat entering the CV and negative values leaving the CV. Due to the definition of the CV boundaries, lateral fluxes only occur on the right face for CV up and on the left side for CV down.

450 warming and the reduced effective thermal conductivity observed on the uphill side of the domain, which combined should yield a decreased heat flux.

Advective heat flux magnitudes are generally much smaller than diffusive flux magnitudes (Fig. 8). Note that advective fluxes only occur in summer and during freeze-up, i.e. when unfrozen water is available for flow, and further only occur [in lateral direction](#) for the sloped cases (steep and medium); the flat case exhibits zero values for advective (lateral) flux, as expected.

455 Note also that the magnitude of lateral advective heat flux is about one order of magnitude larger on the downhill side (Fig. 8b, dashed) than on the uphill side (Fig. 8b, solid).

As water flows and accumulates downhill, the heat carried by water causes the lateral heat flux magnitude to increases downhill. This can be seen by the flux magnitude across the $x=2$ m face (Fig. 8b, uphill) being much smaller than across the $x=48$ m face (Fig. 8b, downhill). Thus, the increase in lateral advective heat flux should contribute to warmer ground 460 temperatures on the downslope side of the domain. However, summer temperature differences between the up- and downhill column show that the downhill columns ($x=48-50$ m) are in fact [mostly](#) cooler, rather than warmer (see Fig. 3a,b). Therefore, we conclude that the lateral advective heat flux, although present, is not sufficient to increase ground temperatures on the downhill side of the domain. [Therefore, another](#) [Another](#) mechanism must be active which [inhibits this small warming, and](#)

465 ~~also~~ causes the downhill side to cool. This implies that the lateral flow of water, which carries heat, has a negligible effect on the warming towards downhill, based on the model configuration and ~~weather forcing assumed~~ hydroclimatic conditions used.

466 ~~Finally~~ Next, consider vertical advection across the near-surface face at ~~0.1~~ 0.1 m depth (Fig. 8a), which is strongly influenced by the uphill vs. downhill side along the hillslope. While the flat case shows values varying around +/- 0.005 W m⁻² in summer, i.e. corresponding to negligible ~~net~~ heat flux, the sloped cases have consistently positive values on the uphill side (~~solid~~ heat entering ground, ~~solid~~ lines) and consistently negative on the downhill side (~~dashed~~ heat leaving ground, ~~dashed~~ lines) during the same period. This gain and loss of heat on the top CV face ($z=0.1$ m) can be explained by surface precipitation (positive, i.e. heat gain) and evaporation (negative, i.e. heat loss). The positive heat flux on the uphill side is dominated by infiltration. As this is the driest part of the transect, it provides less moisture available for evaporative cooling. This energy flux directed towards the subsurface ~~together with an overall lower heat capacity~~ explains why the uphill part of the transect is warmer during summer (Fig. 4, upper panels). The negative flux on the downhill side is a result of ~~higher liquid saturation~~ 475 ~~providing more water for~~ evaporation, which transports water and heat upwards out of the model (i.e. ~~corresponding to heat lost to the atmosphere~~ evaporative cooling). Evaporative flux ~~as well as net infiltration (P-ET)~~ directly at the surface ($z=0$ m) is given in Fig. S3-S6 in the supplementary material. ~~In deeper layers of the active layer (i.e. the bottom face), positive advective heat flux transports energy and heat towards the surface (Fig. 8d, dashed lines), which can explain the positive values (slope is warmer than the flat case) in Fig. 3d,f. In the uphill CV (Fig. 8d, solid lines), energy keeps getting transported down into deeper layers, contributing to warmer temperatures in the lower active layer.~~

480

3.5 Combined mass and energy fluxes

To further understand how much energy is carried by ~~laterally~~ seeping water, we compare the lateral advected energy flux on the left or right faces of the CVs ~~alongside the (corresponding to Fig. 8b and c) alongside the lateral~~ water mass flux on the same faces, and compare the timing of peaks (Fig. 9; a complete presentation of the mass fluxes across all faces is provided in 485 Fig. S4-S7 in the supplementary material). Note that units between advective heat flux and mass flux are different and that the following interpretation focuses on the shape of the curves, rather than absolute values.

As can be seen (Fig. 9), advective heat flux (blue) peaks before September in both uphill and downhill CVs ~~in both slopes~~ and declines shortly after. Mass flux (yellow) also has its first peak before September, but with prolonged duration of flow and declines ~~gradually~~.

490 ~~Daily advective energy flux and mass flux (7-day moving average) through the faces of the uphill (a,e) and downhill (b,d) CV. Note that the fluxes have different units. The sign convention adopted is positive values represent heat entering the CV and negative values leaving the CV.~~

~~more gradually.~~ For the uphill CV, it can be seen that advective heat flux is close to zero already by ~~the end of September~~ October, while mass flux reaches zero only by mid November. The downhill CVs exhibit a second, less distinct mass flux peak just before and during freeze-up in the end of October, which is however not associated with a peak in advective heat flux. ~~This indicates~~

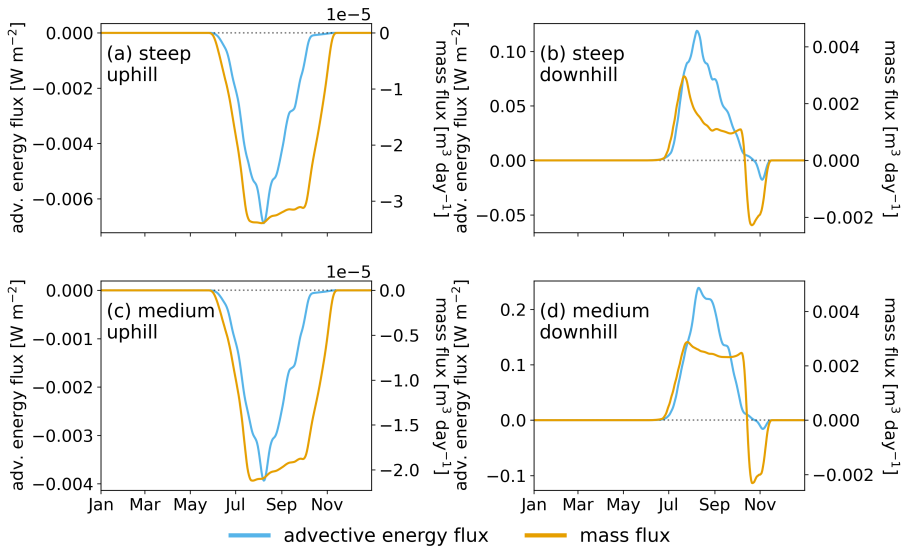


Figure 9. Daily advective energy flux (blue) and mass flux (orange) through the faces of the uphill (a,c) and downhill (b,d) CV. Daily values are averaged over a 7-day window. Note that the fluxes have different units. The sign convention adopted is positive values represent heat entering the CV and negative values leaving the CV.

The findings from both CVs indicate that heat is being carried with water flow during the warm season, corresponding to mid-thaw period, but little advective heat is being transported by the end of the thaw season. This is caused by the permafrost acting as a significant heat sink and reservoir for cooling of the soil column above. Infiltrating water from the surface gets cooled down rapidly causing it to attain equilibrium with its surroundings. Then, although water seepage and flow occurs, it does not contribute much to advective heat transport, as the flowing water is at the same temperature as its surroundings.

During Note also that during freeze-up (November), moisture movement uphill can be seen in the downhill CVs, there are negative values for mass flux (Fig. 9b,d, negative values), indicating moisture is leaving the CV in the uphill direction, which is indicative of lateral cryosuction.

505 3.6 Impact of changes in precipitation

In order to investigate the effects of reduced or increased precipitation, two additional wetness scenarios are considered for each hillside; a dry hillslope; an even drier scenario (S0R0) and a scenario with increased wetness (S2R2). Snow (S) and rain (R) precipitation rates are set to 0 for S0R0, resulting in a completely dry climate, and the rates are multiplied by 2 in the S2R2 scenario, resulting in a climate that is twice as wet as the current climate. We compare the scenarios with regard to temperature differences, active layer thickness, and timing of freeze-up, and advective energy flux.

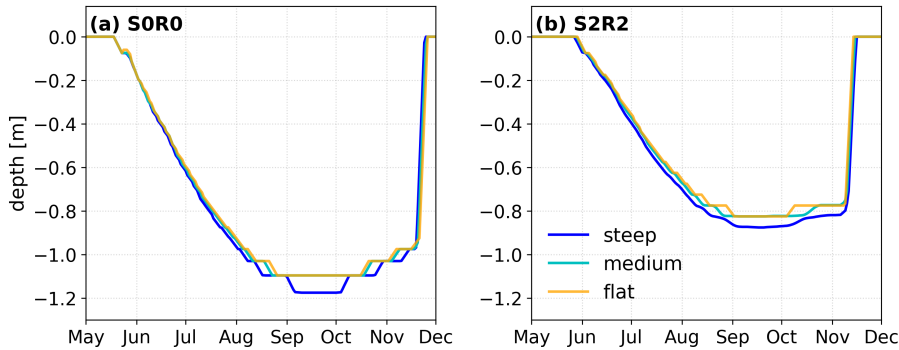


Figure 10. Representation of thaw depth compared between the steep (blue), medium (cyan) and flat case (yellow) as daily, spatially averaged thaw depth temporally averaged over a 5-day window from May to December in the last year of the simulation. Note that thaw depth is defined as cells within the model domain that exceed 0°C . **a** shows the results for the SOR0 (dry) scenario, while **b** shows daily thaw depths for the S2R2 (wet) scenario.

Firstly, we find that both slopes and the flat case are notably warmer in the no-precipitation scenario (SOR0) and colder in the doubled precipitation scenario (S2R2) scenario (not shown). Relative temperature differences between the slopes are generally in a similar range as in the original precipitation scenario with the exception of the downhill side (last column of the domain) in the S2R2 scenario being even colder. On October 28, the downhill side is as much as -1.3°C colder in the steep case compared to the flat case, while the original precipitation scenario showed a maximum difference of -0.25°C on the same day. In the dry SOR0 scenario the difference is only -0.09°C on the same day between the steep and the flat case. A similar pattern can be seen consistently throughout the year.

Active layer thickness further support these findings (Fig. 10). Maximum active layer thickness is deepest in the scenario with no precipitation (steep: 0.9751.18 m, medium and flat: 0.9251.1 m), while it is the shallowest in the doubled precipitation scenario (steep: 0.6250.88 m, medium and flat: 0.5750.825 m) (supplementary material Fig. S5 and Fig. S6). Note that the difference in absolute maximum active layer thickness between the medium and flat slope is very small averaged throughout the transect. Due to the temperature difference, however, the medium case experiences an earlier thaw and delayed freeze-up in the sensitivity scenarios as well as in the original scenario.

The timing of thaw and freeze-up is different throughout the inclinations in each scenario. In the original scenario, all cases start thawing by May 24 and are fully frozen again on November 20. While in the scenario with no precipitation (SOR0) also shows the latest, thaw has started in May 18 for the medium and flat case (the steep case on May 24), and freeze-up on November 20, it is complete on November 21. In S2R2 thaw begins on May 27 in the medium and flat case and May 29 in the steep case, while the last day with unfrozen subsurface-cells is November 3, about 11, almost two weeks earlier than in the other two scenarios. Overall, the scenarios show that the higher the amount of recharge added through precipitation on the surface, the lower the ground temperatures will be in the both the sloped cases as well as the flat case. Note that multiplying snow by a factor of 2 still did not result in a snow cover significant enough to have an insulating effect on the subsurface.

We attribute the temperature difference of the original scenario to the effect of changes in heat capacity and increased/decreased moisture availability for evaporative cooling in the wetter and drier scenario, respectively (not shown). These results are consistent with previously observed cooling effect of precipitation on the active layer. Wen et al. (2014) and Wu and Zhang (2008) both documented a cooling of the active layer in response to rainfall on the Tibetan Plateau. In contrast, e.g., Douglas et al. (2020) and Mekonnen et al. (2021) found a warming effect of summer precipitation on active layer temperatures. However, those studies ~~do~~ did not account for the influences of topography.

As for heat fluxes along the faces of the CVs, we find that most fluxes follow the overall observed patterns in the original simulation depending on moisture content. For instance, diffusive heat flux in summer near the surface is lowest in the dry case S0R0 due to lower saturation, highest in the wetter case S2R2, and with the original precipitation scenario located in between. Vertical advection, i.e. heat carried by infiltration and/or evaporation processes, show that additional moisture in the downhill column further increase evaporation. However, while upwards advective heat flux in the steep case in the original scenario has a maximum of $\sim 0.1 \text{ W m}^{-2}$, it increases by a factor of three to $\sim 0.3 \text{ W m}^{-2}$ in the S2R2 case. This likely leads to an even greater evaporative cooling effect in the downhill column. A similar non-linear development can be seen in lateral advective heat flux. Although still very small in absolute values, lateral advection also increases by a factor of three between the original and the S2R2 case from ~ 0.04 to $\sim 0.12 \text{ W m}^{-2}$.

These findings imply that potential future changes in air temperatures and precipitation towards a warmer and wetter climate could have opposing effects on subsurface temperatures. While higher summer temperatures have a high potential to increase active layer thickness in a catchment, higher precipitation amounts could counteract these processes and act as a heat sink.

Therefore, the interaction of warmer temperatures and increased precipitation rates under change climates warrants investigation. Moreover, a transient development of a combined temperature and precipitation scenario is likely to yield a different result than our step-wise increase of precipitation alone. Potentially, a deeper active layer might lead to a greater volume of unfrozen soil and water, which is available for energy transport (Walvoord and Kurylyk, 2016). This could then lead to even higher non-linearly increasing advective heat fluxes that could eventually contribute to the energy budget downhill.

3.7 Further implications Outlook

Our study has shown that there are differences in the thermal-hydraulic state of the subsurface between the uphill and the downhill side of a 50 m long hillslope transect. Vertical advective heat fluxes (infiltration and evaporative cooling) play a major role in this comparison causing a great share of the differences between the flat control case and the slopes. Evaporative cooling has previously been identified as one of the major non-conductive heat fluxes causing a subsurface cooling in permafrost landscapes (Kane et al., 2001; Wu and Zhang, 2008; Wen et al., 2014; Li et al., 2019; Luo et al., 2020). Lateral advective heat flux in this continuous, high Arctic permafrost landscape with generally low hydraulic conductivity and low precipitation amounts is not sufficient to increase temperatures downhill, corresponding to e.g., a valley bottom. In fact, we observe a contrary effect, such that lateral flow increases moisture content downhill, contributing to enhanced evaporation and evaporative cooling downhill.

Other advancements in 2D permafrost modeling have previously shown that lateral flow of water and associated advection of heat in sub-Arctic, discontinuous permafrost landscapes can significantly change the temperature regime of the subsurface as well as the timing of thaw and freeze-up (Sjöberg et al., 2016). Shojae Ghias et al. (2019) and McKenzie and Voss (2013) also showed in several model setups that a combined conduction-advection scenario causes an increased permafrost thaw as opposed to a conduction-only scenario. This highlights how different advective heat transport affects different landscapes. Under conditions with lower hydraulic conductivity within, highlighting the importance of lateral heat advection. In a polygonal tundra, continuous permafrost landscape setup, model results by Abolt et al. (2020) show that temperature differences within a single polygon are caused by moisture redistribution. While the rims where drier and warmer, the subsurface and no topography, advective heat flux has found to not have such a significant impact on the temperature regime (Kurylyk et al., 2016) centers showed colder temperatures. This is attributed to heat capacity and evaporative cooling, which is in line with our findings. This implies that processes found in our study are more relevant for a high-Arctic hillslope setting low in dry areas and high in wet areas. Accordingly, lateral energy fluxes are governed by lateral conduction and temperature gradients. Even though this is on a much smaller scale than our hillslope simulations, it shows similar governing effects of temperature distribution as in the present study and highlights the importance of lateral processes not only in the form of heat advection. Evaporative cooling has previously been identified as one of the major non-conductive heat fluxes causing a subsurface cooling in permafrost landscapes (Kane et al., 2001; Wu and Zhang, 2008; Wen et al., 2014; Li et al., 2019; Luo et al., 2020).

The observed downhill-cooling effect

The observed temperature differences between uphill and downhill of up to about 1.20.80 °C for steep (22°) and 0.60.56 °C for medium (11°) inclinations slopes in the present study is obtained for a model domain with a lateral distance of 50 m. We generalize these results by calculating lateral and vertical (x -direction) and vertical (z -direction) cooling rates based on the slope inclinations. For the steep slope case, this results in a lateral cooling rate of 0.0260.016 °C/m and a vertical cooling rate of 0.0650.04 °C/m. For the medium slope, the lateral cooling rate amounts to 0.0150.01 °C/m. The vertical cooling rate is slightly higher (0.075 higher (0.056 °C/m) than in the steep slope case. These rates are representative for slopes in the Adventdalen area in Svalbard under current climatic conditions.

Projecting these results to larger scales, hillslope processes might cause significant differences in permafrost distributions throughout a catchment. As shown in Fig. 1, slope inclinations described in this study are present in almost all regions throughout the Arctic and therefore should be accounted for in larger-scale permafrost models. Besides Svalbard, other regions such as Greenland, Yukon, and the Russian Far Eastern Federal District show a considerable share of slopes within the steepness-range simulated in this study. Since our slopes were limited to 50 m in horizontal distance, it can be expected that longer slopes enhance desaturation uphill and aggregate more water towards the downhill side, eventually leading to fully saturated conditions and surface water formation at the slope base. At the same time, lateral advective heat fluxes have shown to increase non-linearly with increasing precipitation, which might also be observable in larger scale hillslope systems due to higher water availability. Considering a full, 3D representation of a hillslope, it is likely that the micro topography within the slope causes further concentration of moisture, eventually leading to water tracks, which have shown to act as conduits for

groundwater even if the adjacent hillslope is already frozen (Evans et al., 2020). These features might substantially change the observed effects in this homogeneous 2D representation of a hillslope without micro topography.

Furthermore, applying this model in a wetter environment or considering potential climate change scenarios towards a wetter climate, new effects of water redistribution might become visible. Ponding water on the downslope side of the domain or in the valley bottom can start forming a talik when energy requirements for the phase change from water to ice (latent heat) become too high. At the same time, higher thermal conductivity leads to greater heat loss towards the subsurface. These competing effects have been studied by Atchley et al. (2016) in a 1D column model, and found that these processes potentially cancel each other out. Clayton et al. (2021) also found that both these processes can be active at the same time in different depths. Furthermore, considering the shallow snow cover in the present study, a potential greater snow cover can lead to insulation effects, which can (i) further increase the effect of uphill warming by insulating the overall warmer soil from cold air temperatures, (ii) provide more water to the subsurface during snow melt and increase evaporative cooling also in the uphill part of the slope, and/or (iii) insulate a potential talik in the downhill part of the domain if enough liquid water is available in summer.

4 Conclusions

This study shows that there are differences in the thermal-hydraulic state of the subsurface between the uphill and the downhill side of a 50 m long hillslope transect, with the uphill area being warmer and the downhill area being colder when compared to each other. Vertical advective heat fluxes (infiltration and evaporative cooling) and both, heat capacity and thermal conductivity, play a major role in this comparison causing a great share of the differences between the flat control case and the sloped cases. The warming effect is strong enough to increase end-of-season active layer depth by 5.5 cm between the flat and the steep case.

Based on the objectives and investigation questions outlined in this study, the main conclusions are as follows.

(i) Hillslope inclination causes differences in ground temperature uphill and downhill. We found that ~~downhill~~ uphill sides are generally ~~cooler than uphill~~ warmer than downhill sides. This ~~downhill cooling~~ uphill warming effect is up to about ~~1.20~~ 0.80 °C for steep (22°) and ~~0.60~~ 0.56 °C for medium (11°) inclinations across a lateral distance of 50 m representative for valleys in Adventdalen, Svalbard.

(ii) The steep slope causes ground warming on the uphill section ~~powerful~~ strong enough to increase maximum active layer depth by ~~55.5~~ cm (~~0.81~~ 0.03 m) as compared to the flat case (~~0.75~~ 0.975 emm). The medium slope, ~~on the other hand, does not incur sufficient warming uphill to significantly increase thaw depth only~~ incurs sufficient uphill warming to increase maximum thaw depth by 1 cm compared to the flat case (~~maximum active layer depth is 0.986 m~~). However, the total volume of unfrozen soil during the warm season increased by ~~5.71~~ 7.7 % in the steep slope case, and ~~1.20~~ 6 % in the medium slope case.

(iii) The uphill warming and slight downhill cooling phenomena observed here ~~is~~ are determined to be caused by ~~two~~ three main processes:

1. Higher moisture content downhill ~~than uphill~~ due to gravitational flow and water accumulation from uphill, which increases effective thermal conductivity and associated heat loss to the atmosphere ~~in winter~~
downhill in winter and slightly less heat loss in winter in the uphill section.
2. Lower moisture in the uphill section decreases heat capacity, which leads to faster warming, while higher moisture content in the downhill section increases heat capacity and slows summer warming down.
3. In summer, higher moisture content downhill causes higher rates of evaporation resulting in greater evaporative cooling compared to the uphill side, where ~~infiltrating precipitation actually outweighs evaporation and actually adds energy to the system~~
evaporative cooling is limited by the dry conditions uphill, leading to relative heat gain through infiltration compared to the downhill side.

We found that temperature difference effect from a flat case, over a medium steep slope (11°) to a steep slope (22°) is not strictly linear and does not double between the two sloped cases. ~~Lateral heat advection, i.e. energy carried by flowing water, only plays a minor role for the temperature differences between uphill and downhill.~~

While active layer thickness increases by more than 5 cm between the steep and the flat case, the medium slope only experiences a 1 cm deeper active layer. This finding, although based on numerical physically-based ~~modelling~~modeling, should be observable in field conditions for this type of environment and hydroclimatic conditions. It highlights the relevance of considering lateral flow of water in the subsurface combined with heat flux for ~~modelling~~modeling arctic catchments with permafrost. It also has implications for interpretation of thermal measurements and time series logging in hillslopes.

Code and data availability. The Advanced Terrestrial Simulator(ATS) (Coon et al., 2019) is open source under the BSD 3-clause license and is publicly available at <https://github.com/amanzi/ats> (last access: July 2020). Simulations were conducted using version 0.88. Forcing datasets and input files are available at https://github.com/a-hamm/ats_hillslope2021.git. Weather data to create the forcing dataset was downloaded from the UNIS website (<https://www.unis.no/resources/weather-stations/>) (last access March 2020) and from the Norwegian Meteorological Institute (<https://www.eklima.met.no>) (last access March 2020).

Author contributions. Both authors conceived the initial conceptualization. Model simulations were performed by AH with guidance from AF. AH wrote the manuscript with contribution from AF.

Competing interests. The authors declare that they have no conflict of interest.

Acknowledgements. This work is funded by Formas (project 2017-00736) with support from the Bolin Centre for Climate Research. We highly appreciate the valuable comments from two anonymous reviewers, which greatly helped to improve the quality of the work. The authors also thank Ahmad Jan and Ethan Coon for technical support with ATS.

- Abolt, C. J., Young, M. H., Atchley, A. L., Harp, D. R., and Coon, E. T.: Feedbacks Between Surface Deformation and Permafrost Degradation in Ice Wedge Polygons, Arctic Coastal Plain, Alaska, *Journal of Geophysical Research: Earth Surface*, 125, <https://doi.org/10.1029/2019JF005349>, <https://onlinelibrary.wiley.com/doi/abs/10.1029/2019JF005349>, 2020.
- Atchley, A. L., Painter, S. L., Harp, D. R., Coon, E. T., Wilson, C. J., Liljedahl, A. K., and Romanovsky, V. E.: Using field observations to inform thermal hydrology models of permafrost dynamics with ATS (v0.83), *Geoscientific Model Development*, 8, 2701–2722, <https://doi.org/10.5194/gmd-8-2701-2015>, <https://www.geosci-model-dev.net/8/2701/2015/>, 2015.
- Atchley, A. L., Coon, E. T., Painter, S. L., Harp, D. R., and Wilson, C. J.: Influences and interactions of inundation, peat, and snow on active layer thickness, *Geophysical Research Letters*, 43, 5116–5123, <https://doi.org/10.1002/2016GL068550>, <https://onlinelibrary.wiley.com/doi/abs/10.1002/2016GL068550>, 2016.
- 670 Biskaborn, B. K., Smith, S. L., Noetzli, J., Matthes, H., Vieira, G., Streletskiy, D. A., Schoeneich, P., Romanovsky, V. E., Lewkowicz, A. G., Abramov, A., Allard, M., Boike, J., Cable, W. L., Christiansen, H. H., Delaloye, R., Diekmann, B., Drozdov, D., Etzelmüller, B., Grosse, G., Guglielmin, M., Ingeman-Nielsen, T., Isaksen, K., Ishikawa, M., Johannsson, M., Johannsson, H., Joo, A., Kaverin, D., Kholodov, A., Konstantinov, P., Kröger, T., Lambiel, C., Lanckman, J.-P., Luo, D., Malkova, G., Meiklejohn, I., Moskalenko, N., Oliva, M., Phillips, M., Ramos, M., Sannel, A. B. K., Sergeev, D., Seybold, C., Skryabin, P., Vasiliev, A., Wu, Q., Yoshikawa, K., Zheleznyak, M., and Lantuit, H.: Permafrost is warming at a global scale, *Nature Communications*, 10, 264, <https://doi.org/10.1038/s41467-018-08240-4>, <http://www.nature.com/articles/s41467-018-08240-4>, 2019.
- Chen, L., Fortier, D., McKenzie, J. M., and Sliger, M.: Impact of heat advection on the thermal regime of roads built on permafrost, *Hydrological Processes*, 34, 1647–1664, <https://doi.org/10.1002/hyp.13688>, <https://onlinelibrary.wiley.com/doi/abs/10.1002/hyp.13688>, 2020.
- 675 Clayton, L. K., Schaefer, K., Battaglia, M. J., Bourgeau-Chavez, L., Chen, J., Chen, R. H., Chen, A. C., Bakian-Dogaheh, K., Grelit, S., Jafarov, E., Liu, L., Michaelides, R. J., Moghaddam, M., Parsekian, A., Rocha, A. V., Schaefer, S. R., Sullivan, T., Tabatabaeenejad, A., Wang, K., Wilson, C. J., Zebker, H. A., Zhang, T., and Zhao, Y.: Active layer thickness as a function of soil water content, *Environmental Research Letters*, <https://doi.org/10.1088/1748-9326/abfa4c>, <https://iopscience.iop.org/article/10.1088/1748-9326/abfa4c>, 2021.
- 680 Coon, E., Svyatsky, D., Jan, A., Kikinzon, E., Berndt, M., Atchley, A., Harp, D., Manzini, G., Shelef, E., Lipnikov, K., Garimella, R., Xu, C., Moulton, D., Karra, S., Painter, S., Jafarov, E., and Molins, S.: Advanced Terrestrial Simulator, <https://doi.org/10.11578/DC.20190911.1>, <https://www.osti.gov/doe/28622>, language: en, 2019.
- 685 Coon, E. T., David Moulton, J., and Painter, S. L.: Managing complexity in simulations of land surface and near-surface processes, *Environmental Modelling & Software*, 78, 134–149, <https://doi.org/10.1016/j.envsoft.2015.12.017>, <https://linkinghub.elsevier.com/retrieve/pii/S1364815215301316>, 2016.
- 690 de Grandpré, I., Fortier, D., and Stephani, E.: Degradation of permafrost beneath a road embankment enhanced by heat advected in groundwater, *Canadian Journal of Earth Sciences*, 49, 953–962, <https://doi.org/10.1139/e2012-018>, <http://www.nrcresearchpress.com/doi/10.1139/e2012-018>, 2012.
- Douglas, T. A., Turetsky, M. R., and Koven, C. D.: Increased rainfall stimulates permafrost thaw across a variety of Interior Alaskan boreal ecosystems, *npj Climate and Atmospheric Science*, 3, 28, <https://doi.org/10.1038/s41612-020-0130-4>, <http://www.nature.com/articles/s41612-020-0130-4>, 2020.

- 695 Evans, S. G. and Ge, S.: Contrasting hydrogeologic responses to warming in permafrost and seasonally frozen ground hillslopes: Hydrogeology of Warming Frozen Grounds, *Geophysical Research Letters*, <https://doi.org/10.1002/2016GL072009>, <http://doi.wiley.com/10.1002/2016GL072009>, 2017.
- 700 Evans, S. G., Godsey, S. E., Rushlow, C. R., and Voss, C.: Water Tracks Enhance Water Flow Above Permafrost in Upland Arctic Alaska Hillslopes, *Journal of Geophysical Research: Earth Surface*, 125, <https://doi.org/10.1029/2019JF005256>, <https://onlinelibrary.wiley.com/doi/abs/10.1029/2019JF005256>, 2020.
- Frampton, A. and Destouni, G.: Impact of degrading permafrost on subsurface solute transport pathways and travel times, *Water Resources Research*, 51, 7680–7701, <https://doi.org/10.1002/2014WR016689>, <https://onlinelibrary.wiley.com/doi/10.1002/2014WR016689>, 2015.
- 705 Frampton, A., Painter, S., Lyon, S. W., and Destouni, G.: Non-isothermal, three-phase simulations of near-surface flows in a model permafrost system under seasonal variability and climate change, *Journal of Hydrology*, 403, 352–359, <https://doi.org/10.1016/j.jhydrol.2011.04.010>, <https://linkinghub.elsevier.com/retrieve/pii/S0022169411002502>, 2011.
- Frampton, A., Painter, S. L., and Destouni, G.: Permafrost degradation and subsurface-flow changes caused by surface warming trends, *Hydrogeology Journal*, 21, 271–280, <https://doi.org/10.1007/s10040-012-0938-z>, <http://link.springer.com/10.1007/s10040-012-0938-z>, 2013.
- 710 Frauenfeld, O. W., Zhang, T., Barry, R. G., and GilichinskySoil, D.: Interdecadal changes in seasonal freeze and thaw depths in Russia, *Journal of Geophysical Research*, 109, D05 101, <https://doi.org/10.1029/2003JD004245>, <http://doi.wiley.com/10.1029/2003JD004245>, 2004.
- Førland, E. J. and Hanssen-Bauer, I.: Increased Precipitation in the Norwegian Arctic: True or False?, *Climatic Change*, 46, 485–509, <https://doi.org/10.1023/A:1005613304674>, <http://link.springer.com/10.1023/A:1005613304674>, 2000.
- Hanssen-Bauer, I., Førland, E., Hisdal, H., Mayer, S., Sandø, A., and Sorteberg, A.: Climate in Svalbard 2100 – a knowledge base for climate adaptation, *Tech. Rep. 1/2019*, Norwegian Centre for Climate Services, 2018.
- 715 Hugelius, G., Strauss, J., Zubrzycki, S., Harden, J. W., Schuur, E. A. G., Ping, C.-L., Schirrmeyer, L., Grosse, G., Michaelson, G. J., Koven, C. D., O'Donnell, J. A., Elberling, B., Mishra, U., Camill, P., Yu, Z., Palmtag, J., and Kuhry, P.: Estimated stocks of circumpolar permafrost carbon with quantified uncertainty ranges and identified data gaps, *Biogeosciences*, 11, 6573–6593, <https://doi.org/10.5194/bg-11-6573-2014>, <https://www.biogeosciences.net/11/6573/2014/>, 2014.
- Iijima, Y., Fedorov, A. N., Park, H., Suzuki, K., Yabuki, H., Maximov, T. C., and Ohata, T.: Abrupt increases in soil temperatures following increased precipitation in a permafrost region, central Lena River basin, Russia, *Permafrost and Periglacial Processes*, 21, 30–41, <https://doi.org/10.1002/ppp.662>, <http://doi.wiley.com/10.1002/ppp.662>, 2010.
- 720 Isaksen, K., Sollid, J. L., Holmlund, P., and Harris, C.: Recent warming of mountain permafrost in Svalbard and Scandinavia, *Journal of Geophysical Research*, 112, F02S04, <https://doi.org/10.1029/2006JF000522>, <http://doi.wiley.com/10.1029/2006JF000522>, 2007.
- Jafarov, E. E., Coon, E. T., Harp, D. R., Wilson, C. J., Painter, S. L., Atchley, A. L., and Romanovsky, V. E.: Modeling the role of preferential 725 snow accumulation in through talik development and hillslope groundwater flow in a transitional permafrost landscape, *Environmental Research Letters*, 13, 105 006, <https://doi.org/10.1088/1748-9326/aadd30>, <http://stacks.iop.org/1748-9326/13/i=10/a=105006?key=crossref.ea8d38a9a41cbb120144acdd5d1d4d37>, 2018.
- Jan, A. and Painter, S. L.: Permafrost thermal conditions are sensitive to shifts in snow timing, *Environmental Research Letters*, 15, 084 026, <https://doi.org/10.1088/1748-9326/ab8ec4>, <https://iopscience.iop.org/article/10.1088/1748-9326/ab8ec4>, 2020.
- 730 Kane, D. L., Hinkel, K. M., Goering, D. J., Hinzman, L. D., and Outcalt, S. I.: Non-conductive heat transfer associated with frozen soils, *Global and Planetary Change*, 29, 275–292, [https://doi.org/10.1016/S0921-8181\(01\)00095-9](https://doi.org/10.1016/S0921-8181(01)00095-9), <https://linkinghub.elsevier.com/retrieve/pii/S0921818101000959>, 2001.

- Karra, S., Painter, S. L., and Lichtner, P. C.: Three-phase numerical model for subsurface hydrology in permafrost-affected regions (PFLOTRAN-ICE v1.0), *The Cryosphere*, 8, 1935–1950, <https://doi.org/10.5194/tc-8-1935-2014>, <https://www.the-cryosphere.net/8/1935/2014/>, 2014.
- Koven, C. D., Ringeval, B., Friedlingstein, P., Ciais, P., Cadule, P., Khvorostyanov, D., Krinner, G., and Tarnocai, C.: Permafrost carbon-climate feedbacks accelerate global warming, *Proceedings of the National Academy of Sciences*, 108, 14 769–14 774, <https://doi.org/10.1073/pnas.1103910108>, <http://www.pnas.org/cgi/doi/10.1073/pnas.1103910108>, 2011.
- Kurylyk, B. L., Hayashi, M., Quinton, W. L., McKenzie, J. M., and Voss, C. I.: Influence of vertical and lateral heat transfer on permafrost thaw, peatland landscape transition, and groundwater flow: Permafrost thaw, landscape change and groundwater flow, *Water Resources Research*, 52, 1286–1305, <https://doi.org/10.1002/2015WR018057>, <http://doi.wiley.com/10.1002/2015WR018057>, 2016.
- Langford, J. E., Schincariol, R. A., Nagare, R. M., Quinton, W. L., and Mohammed, A. A.: Transient and Transition Factors in Modeling Permafrost Thaw and Groundwater Flow, *Groundwater*, 58, 258–268, <https://doi.org/10.1111/gwat.12903>, <https://onlinelibrary.wiley.com/doi/abs/10.1111/gwat.12903>, 2020.
- Li, D.-s., Wen, Z., Cheng, Q.-g., Xing, A.-g., Zhang, M.-l., and Li, A.-y.: Thermal dynamics of the permafrost active layer under increased precipitation at the Qinghai-Tibet Plateau, *Journal of Mountain Science*, 16, 309–322, <https://doi.org/10.1007/s11629-018-5153-5>, <http://link.springer.com/10.1007/s11629-018-5153-5>, 2019.
- Loranty, M. M., Abbott, B. W., Blok, D., Douglas, T. A., Epstein, H. E., Forbes, B. C., Jones, B. M., Kholodov, A. L., Kropp, H., Malhotra, A., Mamet, S. D., Myers-Smith, I. H., Natali, S. M., O'Donnell, J. A., Phoenix, G. K., Rocha, A. V., Sonnentag, O., Tape, K. D., and Walker, D. A.: Reviews and syntheses: Changing ecosystem influences on soil thermal regimes in northern high-latitude permafrost regions, *Biogeosciences*, 15, 5287–5313, <https://doi.org/10.5194/bg-15-5287-2018>, <https://bg.copernicus.org/articles/15/5287/2018/>, 2018.
- Luo, D., Jin, H., Bense, V. F., Jin, X., and Li, X.: Hydrothermal processes of near-surface warm permafrost in response to strong precipitation events in the Headwater Area of the Yellow River, Tibetan Plateau, *Geoderma*, 376, 114 531, <https://doi.org/10.1016/j.geoderma.2020.114531>, <https://linkinghub.elsevier.com/retrieve/pii/S0016706120306704>, 2020.
- McGuire, A. D., Anderson, L. G., Christensen, T. R., Dallimore, S., Guo, L., Hayes, D. J., Heimann, M., Lorenson, T. D., Macdonald, R. W., and Roulet, N.: Sensitivity of the carbon cycle in the Arctic to climate change, *Ecological Monographs*, 79, 523–555, <https://doi.org/10.1890/08-2025.1>, <http://doi.wiley.com/10.1890/08-2025.1>, 2009.
- McKenzie, J. M. and Voss, C. I.: Permafrost thaw in a nested groundwater-flow system, *Hydrogeology Journal*, p. 18, 2013.
- McKenzie, J. M., Kurylyk, B. L., Walvoord, M. A., Bense, V. F., Fortier, D., Spence, C., and Grenier, C.: Invited perspective: What lies beneath a changing Arctic?, *The Cryosphere*, 15, 479–484, <https://doi.org/10.5194/tc-15-479-2021>, <https://tc.copernicus.org/articles/15/479/2021/>, 2021.
- Mekonnen, Z. A., Riley, W. J., Grant, R. F., and Romanovsky, V. E.: Changes in precipitation and air temperature contribute comparably to permafrost degradation in a warmer climate, *Environmental Research Letters*, 16, 024 008, <https://doi.org/10.1088/1748-9326/abc444>, <https://iopscience.iop.org/article/10.1088/1748-9326/abc444>, 2021.
- Painter, S. L.: Three-phase numerical model of water migration in partially frozen geological media: model formulation, validation, and applications, *Computational Geosciences*, 15, 69–85, <https://doi.org/10.1007/s10596-010-9197-z>, <http://link.springer.com/10.1007/s10596-010-9197-z>, 2011.
- Painter, S. L. and Karra, S.: Constitutive Model for Unfrozen Water Content in Subfreezing Unsaturated Soils, *Vadose Zone Journal*, 13, vzzj2013.04.0071, <https://doi.org/10.2136/vzzj2013.04.0071>, <http://doi.wiley.com/10.2136/vzzj2013.04.0071>, 2014.

- 770 Painter, S. L., Coon, E. T., Atchley, A. L., Berndt, M., Garimella, R., Moulton, J. D., Svyatskiy, D., and Wilson, C. J.: Integrated surface/sub-surface permafrost thermal hydrology: Model formulation and proof-of-concept simulations, *Water Resources Research*, 52, 6062–6077, <https://doi.org/10.1002/2015WR018427>, <http://doi.wiley.com/10.1002/2015WR018427>, 2016.
- Porter, C., Morin, P., Howat, I., Noh, M.-J., Bates, B., Peterman, K., Keesey, S., Schlenk, M., Gardiner, J., Tomko, K., Willis, M., Kelleher, C., Cloutier, M., Husby, E., Foga, S., Nakamura, H., Platson, M., Wethington, M., Williamson, C., Bauer, G., Enos, J., Arnold, G., Kramer, 775 Becker, P., Doshi, A., D’Souza, C., Cummins, P., Laurier, F., and Bojesen, M.: ArcticDEM, <https://doi.org/10.7910/dvn/ohhukh>, <https://dataVERSE.harvard.edu/citation?persistentId=doi:10.7910/DVN/OHHUKH>, type: dataset, 2018.
- Riseborough, D., Shiklomanov, N., Etzelmüller, B., Gruber, S., and Marchenko, S.: Recent advances in permafrost modelling, *Permafrost and Periglacial Processes*, 19, 137–156, <https://doi.org/10.1002/ppp.615>, <http://doi.wiley.com/10.1002/ppp.615>, 2008.
- Schuh, C., Frampton, A., and Christiansen, H. H.: Soil moisture redistribution and its effect on inter-annual active layer temperature and 780 thickness variations in a dry loess terrace in Adventdalen, Svalbard, *The Cryosphere*, 11, 635–651, <https://doi.org/10.5194/tc-11-635-2017>, <https://www.the-cryosphere.net/11/635/2017/>, 2017.
- Schuur, E. A. G., McGuire, A. D., Schädel, C., Grosse, G., Harden, J. W., Hayes, D. J., Hugelius, G., Koven, C. D., Kuhry, P., Lawrence, 785 D. M., Natali, S. M., Olefeldt, D., Romanovsky, V. E., Schaefer, K., Turetsky, M. R., Treat, C. C., and Vonk, J. E.: Climate change and the permafrost carbon feedback, *Nature*, 520, 171–179, <https://doi.org/10.1038/nature14338>, <http://www.nature.com/articles/nature14338>, 2015.
- Shojae Ghias, M., Therrien, R., Molson, J., and Lemieux, J.-M.: Numerical simulations of shallow groundwater flow and heat transport in continuous permafrost setting under impact of climate warming, *Canadian Geotechnical Journal*, 56, 436–448, <https://doi.org/10.1139/cgj-2017-0182>, <http://www.nrcresearchpress.com/doi/10.1139/cgj-2017-0182>, 2019.
- Sjöberg, Y., Coon, E., K. Sannel, A. B., Pannetier, R., Harp, D., Frampton, A., Painter, S. L., and Lyon, S. W.: Thermal effects of groundwater 790 flow through subarctic fens: A case study based on field observations and numerical modeling, *Water Resources Research*, 52, 1591–1606, <https://doi.org/10.1002/2015WR017571>, <http://doi.wiley.com/10.1002/2015WR017571>, 2016.
- Strand, S. M., Christiansen, H. H., Johansson, M., Åkerman, J., and Humlum, O.: Active layer thickening and controls on interannual variability in the Nordic Arctic compared to the circum-Arctic, *Permafrost and Periglacial Processes*, p. ppp.2088, <https://doi.org/10.1002/ppp.2088>, <https://onlinelibrary.wiley.com/doi/10.1002/ppp.2088>, 2020.
- 795 Veuille, S., Fortier, D., Verpaelst, M., and Grandmont, K.: Heat Advection in the Active Layer of Permafrost: Physical Modelling to Quantify the Impact of Subsurface Flow on Soil Thawing., in: *GéoQuébec 2015 Proceedings of the 68th Canadian Geotechnical Conference and the 7th Canadian Permafrost Conference*, p. 9, Québec City, Québec, 2015.
- Walvoord, M. A. and Kurylyk, B. L.: Hydrologic Impacts of Thawing Permafrost—A Review, *Vadose Zone Journal*, 15, 0, <https://doi.org/10.2136/vzj2016.01.0010>, <https://dl.sciencesocieties.org/publications/vzj/abstracts/15/6/vzj2016.01.0010>, 2016.
- 800 Wen, Z., Niu, F., Yu, Q., Wang, D., Feng, W., and Zheng, J.: The role of rainfall in the thermal-moisture dynamics of the active layer at Beiluhe of Qinghai-Tibetan plateau, *Environmental Earth Sciences*, 71, 1195–1204, <https://doi.org/10.1007/s12665-013-2523-8>, <http://link.springer.com/10.1007/s12665-013-2523-8>, 2014.
- Westermann, S., Langer, M., Boike, J., Heikenfeld, M., Peter, M., Etzelmüller, B., and Krinner, G.: Simulating the thermal regime and 805 thaw processes of ice-rich permafrost ground with the land-surface model CryoGrid 3, *Geoscientific Model Development*, 9, 523–546, <https://doi.org/10.5194/gmd-9-523-2016>, <https://gmd.copernicus.org/articles/9/523/2016/>, 2016.
- Wu, Q. and Zhang, T.: Recent permafrost warming on the Qinghai-Tibetan Plateau, *Journal of Geophysical Research*, 113, D13 108, <https://doi.org/10.1029/2007JD009539>, <http://doi.wiley.com/10.1029/2007JD009539>, 2008.

- Zhang, T., Osterkamp, T. E., and Stamnes, K.: Effects of Climate on the Active Layer and Permafrost on the North Slope of Alaska, U.S.A., *Permafrost and Periglacial Processes*, 8, 23, 1997.
- 810 Zhang, T., Barry, R. G., Knowles, K., Heginbottom, J. A., and Brown, J.: Statistics and characteristics of permafrost and ground-ice distribution in the Northern Hemisphere ¹, *Polar Geography*, 23, 132–154, <https://doi.org/10.1080/10889379909377670>, <http://www.tandfonline.com/doi/abs/10.1080/10889379909377670>, 1999.
- Zhu, X., Wu, T., Li, R., Xie, C., Hu, G., Qin, Y., Wang, W., Hao, J., Yang, S., Ni, J., and Yang, C.: Impacts of Summer Extreme Precipitation Events on the Hydrothermal Dynamics of the Active Layer in the Tanggula Permafrost Region on the Qinghai-
815 Tibetan Plateau: Impacts of Precipitation on Active Layer, *Journal of Geophysical Research: Atmospheres*, 122, 11,549–11,567, <https://doi.org/10.1002/2017JD026736>, <http://doi.wiley.com/10.1002/2017JD026736>, 2017.